ACS APPLIED BIO MATERIALS

www.acsabm.org
Article

3D Bioprinting of High-Grade Serous Ovarian Cancer Cells: Workflow for Gelatin-Based Bioink Formulation with Hyaluronic Acid and Printability Assessment

Chiara Scrocciolani,[†] Leonardo Caserio,[†] Silvia Grillo, Flavia Ottavi, Ilenia Masi, Emanuela Jacchetti, Francesco Briatico Vangosa, Manuela Teresa Raimondi, Bianca Maria Colosimo, Laura Rosanò, Davide Moscatelli, and Emanuele Mauri*

Cite This: *ACS Appl. Bio Mater.* 2026, 9, 6370−6387

Read Online

ACCESS | Metrics & More | Article Recommendations | Supporting Information

ABSTRACT: Ovarian cancer (OC) is one of the leading causes of cancer-related mortality in women, primarily due to the late-stage diagnosis and limited therapeutic efficacy. Three-dimensional (3D) bioprinting enables the fabrication of cell-laden scaffolds that better recapitulate the native spatial organization and may support the investigation of tumor cell behavior. However, high-grade serous ovarian cancer (HG-SOC) cell subtypes remain largely unexplored in bioprinting, and it remains unclear whether a different scaffold composition is required to provide an optimal niche for each subtype. To address these gaps, we developed a 3D bioprinting workflow based on methacrylated gelatin (GelMA) and a hybrid methacrylated hyaluronic acid/methacrylated gelatin formulation (HAGel) to generate constructs containing KURAMOCHI and OVCAR3 HG-SOC cells, alongside SKOV3 as a reference epithelial OC model. Bioink formulations were optimized to achieve reproducible extrusion printing and stable construct formation. Rheological characterization showed a higher storage modulus for HAGel scaffold (approximately 2-fold higher than GelMA), while both formulations remained within a stiffness range suitable for cell culture. GelMA exhibited higher swelling and a broader printability window, whereas HAGel showed reduced water uptake and required more restricted processing conditions to ensure stable bioprinting. Cellular responses were evaluated in terms of viability, proliferation, morphology, and expression of hyaluronic-acid-associated markers (e.g., CD44, MMP-2, and MMP-14). Postprinting viability remained high throughout culture (approximately 80–99% after 14 days), with outcomes depending on both cell line and hydrogel formulation. KURAMOCHI and SKOV3 cells exhibited higher viability and cell density in HAGel, whereas OVCAR3 cells performed better in GelMA, consistent with CD44 expression and MMP trends, reflecting subtype-dependent interactions with the scaffold composition. These findings demonstrate the feasibility of bioprinting HG-SOC cells and show how bioink formulations may contribute to cell-line-dependent response, paving the way for a rational design of constructs for advanced OC in vitro platforms.

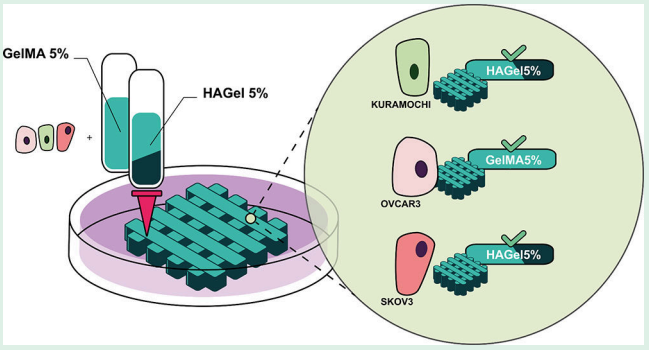

KEYWORDS: *ovarian cancer, high-grade serous ovarian cancer, 3D bioprinting, hyaluronic acid, gelatin*

1. INTRODUCTION

Ovarian cancer (OC) is the eighth worldwide cause of death in women, with a strong impact on life expectancy and more than 300,000 new cases per year documented in the last three years. Early diagnoses remain challenging due to the lack of symptoms during initial stages: only 15.7% of cases are detected at a localized stage, providing a 5-year survival rate of 92.6%, whereas for late-stage conditions, this percentage decreases to 48.6%.[1] For this reason, the development of advanced experimental platforms becomes essential for investigating cell behavior and disease progression, ultimately supporting improvements in diagnosis, prognosis, and therapies.

In this context, 3D culture systems have emerged as more physiologically relevant tools, as they provide a more realistic spatial arrangement of cells and better recapitulate key tumor-associated features, such as oxygen and nutrient gradients, diffusion constraints, homotypic or heterotypic cell−cell interactions.[2] In OC research, conventional 3D culture approaches are primarily

Received: February 12, 2026
Revised: June 1, 2026
Accepted: June 3, 2026
Published: June 26, 2026

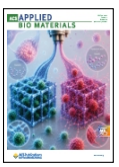

https://doi.org/10.1021/acsabm.6c00299
ACS Appl. Bio Mater. 2026, 9, 6370−6387

based on bulk scaffolds, including Matrigel and hydrogel-based platforms, in which cells are either embedded within or seeded onto the matrix.[3] Matrigel, rich in ECM components, has been widely employed for supporting metastatic growth and studying cancer cell invasion, while both natural materials (such as collagen,[4] gelatin,[5] and alginate[6]) and synthetic hydrogels[7,8] have been extensively used to investigate key mechanisms underlying the tumor progression, including invasion,[9] spheroid formation,[10] and drug response.[11]

For instance, collagen-I hydrogels have been used as suitable matrices for investigating the invasiveness and drug resistance of human OC cell lines derived from primary tumors.[12] In another study, alginate was used as a crosslinking component in the formulation of a polyethylene glycol-poly(methyl vinyl ether) matrix for supporting the long-term growth, proliferation, and spheroid formation of SKOV3 cells.[8]

However, the potential of 3D culture is only partially exploited in bulk matrices, where the lack of customizable architectures restricts the control over the cell distribution and matrix geometry, and the experimental reproducibility.[13,14] To overcome these limitations, 3D bioprinting has emerged as a promising technology enabling the controlled layer-by-layer deposition of cell-laden materials with high spatial precision while preserving cell viability and supporting nutrient exchange between cells and the surrounding microenvironment.

This approach has been successfully applied to several tumor models, including breast, pancreatic, and liver cancers, using bioinks based on collagen, gelatin, alginate, and decellularized ECM, respectively.[15] In OC, however, bioprinting applications remain limited and have mainly focused on recreating multicellular interactions, with comparatively less attention given to the rational design of bioinks and their impact on model functionality. A droplet-based system was employed to pattern OVCAR5 and MRC-5 fibroblasts on a Matrigel scaffold to investigate tumor−stromal interactions and regulatory involved mechanisms,[16] while a 3D extrusion-based technology was utilized to combine SKOV3 cells and cancer-associated fibroblasts (MeWo cells). In this case, cells were cultured into a gelatin-alginate hydrogel, which ensured high viability and proliferation, retaining the expression of key phenotypic markers, such as PAX8 for SKOV3 cells and FAP for MeWo cells.[17] Alongside these progresses in studying cellular interactions within bioprinted models, also the composition and physicochemical properties of the hydrogel bioinks (e.g., stiffness and viscosity) can influence basic cellular outcomes, including viability, proliferation, and overall behavior during and after printing, suggesting that careful optimization of the printable matrix remains a critical step in any bioprinting workflow.[18,19] This aspect is particularly relevant for OC studies, especially for high-grade serous ovarian cancer (HG-SOC), where the tumor cell lines often differ in morphology, growth dynamics, and surrounding environment.[20] As a consequence, a single hydrogel formulation may not uniformly support all OC cell lines, and slight adjustments in matrix composition could be needed to ensure that each line is maintained in an appropriate niche.[21,22] Evaluating how and if modified formulations affect a single tumor cell population represents an essential preliminary step before progressing toward more complex, multicellular bioprinted models. Given the relevance of HG-SOC as the most common and aggressive form of OC, due to the characteristic high metastatic potential and resistance to chemotherapeutics, the development of an optimal niche for the cell subtypes is fundamental to ensure functional adhesion and proliferation in 3D. The investigation of the scaffold formulation as a variable that could affect the specific tumor cell viability and proliferation over time is not discussed in the HG-SOC field.

For these reasons, in this work, we adopted a substrate-focused approach to evaluate printable hydrogel substrates for HG-SOC cells. We propose the validation of two scaffold compositions (i.e., bioink formulations) for the 3D bioprinting of KURAMOCHI and OVCAR3 cells, representative HG-SOC cell lines. We compared the results of cell-laden gelatin-based scaffolds with hybrid matrices of hyaluronic acid (HA) and gelatin. Both macromolecules were functionalized with vinyl groups and used in the corresponding bioink formulations. The scaffolds were 3D printed via an extrusion-based process followed by UV exposure to chemically crosslink the polymer backbone without affecting cell viability, while ensuring the scaffold stability over time. HA was selected due to its role as a major component of the ECM, playing a crucial role in OC microenvironment and promoting cell signaling via interaction with cell surface receptors.[23] This polysaccharide is also associated with poor prognosis in OC, including higher rates of recurrence and a reduced 5-year survival.[24] Despite this relevance, the literature lacks OC models incorporating HA as a scaffold component, favoring other polysaccharides (e.g., chitosan, cellulose, alginate, and agarose) and proteins as material substrates in 2D.

To demonstrate the importance of properly designing the OC cell substrate for biomedical applications, we assessed key scaffold-dependent cell behaviors, such as cell viability and proliferation, alongside the expression levels of HA-sensitive receptors (such as CD44) and additional markers associated with cell−matrix interactions and phenotypic remodeling.

In particular, the variation in cell viability/proliferation and receptor expression was evaluated across the two tested hydrogel formulations to identify the substrate conditions that optimally support the cells after printing.

As a comparison, 3D bioprinting of SKOV3 cells, a widely used reference line for studies of epithelial ovarian cancer (non-HG-SOC), was performed. This study represents the first investigation of 3D bioprinting of HG-SOC cell lines, exploring the potential influence of the hydrogel substrate on cell behavior, and aims to pave the way for the fabrication of 3D OC scaffolds as functional systems for therapeutic research.

2. EXPERIMENTAL SECTION

2.1. Materials

Gelatin type A (Gel, strength 300), phosphate-buffered saline (PBS), methacrylic anhydride (MA), triethylamine (TEA, ≥99.5% v/v), *N*,*N*-dimethylformamide (DMF, ≥99.8% v/v), lithium phenyl-2,4,6-trimethylbenzoylphosphinate (LAP, ≥95%), collagenase type II (Cls II), buffer substance TES, Calcein-AM (≥90%), ethidium homodimer (EthD-1, ≥90%), bisbenzimide H 33342 trihydrochloride (Hoechst, ≥97%), phalloidin-tetramethylrhodamine B isothiocyanate (phalloidin-TRITC, ≥90%), unconjugated polyclonal rabbit antihuman anti-Ki67 antibody, anti-rabbit IgG Alexa Fluor 488 secondary antibody, fetal bovine serum (FBS), paraformaldehyde (PFA), RPMI-1640 culture medium, McCoy's 5A Medium, and penicillin−streptomycin (Pen−Strep) were purchased from Merck KGaA (Darmstadt, Germany). Hyaluronic acid sodium salt (extra low molecular weight 8000−15000, HA) was acquired from Biosynth Carbosynth (Staad, Switzerland), while glycidyl methacrylate (GM, ≥97% v/v) was from Thermo Fisher Scientific (Waltham, MA, USA).

2.2. Methacrylation of Gelatin and Hyaluronic Acid

The conjugation of methacrylic group on Gel and HA backbone was performed following the protocol discussed in our previous work[25] and

https://doi.org/10.1021/acsabm.6c00299
ACS Appl. Bio Mater. 2026, 9, 6370−6387

the method proposed by Sigen et al.[26] Briefly, for methacrylated Gel (GelMA), pure Gel was dissolved at 10% w/v PBS at 50 °C. MA was then added dropwise (0.8 mL/g Gel) and allowed to react for 2 h under stirring. The system was then diluted in warm PBS 1:5 v/v and stirred at 50 °C for 24 h. The functionalized polymer was collected after dialysis against distilled water for 7 days at 50 °C (MWCO: 6−8 kDa, Repligen, USA). For the grafting between glycidyl methacrylate and HA (GMHA), HA (2.0 g, 5.0 mmol) was dissolved in deionized water (100 mL), and an organic solution of GM (35.5 g, 250 mmol) and TEA (25.3 g, 250 mmol) in DMF (100 mL) was added dropwise. The resulting system was stirred for 3 days at room temperature (RT). The polymer solution was purified via dialysis (MWCO: 6−8 kDa, Repligen, USA) against distilled water for 7 days. Finally, GelMA and GMHA were freeze-dried, and the obtained solids were stored at −20 °C until use.

2.3. Polymer Chemical Characterization

2.3.1. NMR. The degree of functionalization (DoF) of GelMA and GMHA was evaluated using ^{1}H NMR spectroscopy (Bruker AC, 400 MHz). The samples were dissolved at a concentration of 10 mg/mL in deuterated water (D_2O), and chemical shifts were reported in parts per million (ppm) relative to TMS as the internal standard. The DoF of GelMA was assessed by comparing the integrals of the methylene peak ascribable to the lysine segment in the reaction product vs the starting Gel. Specifically, DoF was calculated according to the following equation (eq 1):[27]

$$\mathrm{DoF}_{\mathrm{GelMA}}(\%) = \left[1 - \frac{A_{\mathrm{lys}_{\mathrm{GelMA}}}}{A_{\mathrm{lys}_{\mathrm{Gel}}}}\right] \times 100 \quad (1)$$

where $A_{\mathrm{lys}_{\mathrm{GelMA}}}$ and $A_{\mathrm{lys}_{\mathrm{Gel}}}$ represent the peak integration of the signal corresponding to the lysine methylene moieties of GelMA and Gel, respectively. For GMHA, the DoF was evaluated according to eq 2:[26]

$$\mathrm{DoF}_{\mathrm{GMHA}}(\%) = \frac{A_{\mathrm{m}_{\mathrm{GMHA}}}}{\frac{A_{\mathrm{meth}_{\mathrm{HA}}}}{3}} \times 100 \quad (2)$$

where $A_{\mathrm{m}_{\mathrm{GMHA}}}$ represents the characteristic methacrylate peaks of the HA functionalization and $A_{\mathrm{meth}_{\mathrm{HA}}}$ is the signal of the methyl protons of the HA backbone.

2.3.2. ATR-FTIR. Dried polymer specimens were characterized via attenuated total reflectance Fourier transform infrared spectroscopy using an Agilent Cary 630 FTIR spectrometer (Agilent Technologies Italia, Italy). Measurements were conducted with 16 cm^{-1} resolution at RT, and each sample was analyzed in a range from 600 to 4000 cm^{-1}, setting 64 scans per sample.

2.4. Ink Preparation

Two distinct polymer formulations were proposed as ink for the 3D printing of hydrogel scaffolds. The first one was composed of GelMA only, dissolved in PBS at a concentration of 5% w/v at 40 °C, and hereinafter labeled as GelMA ink, while the second one consisted of a blend of GelMA and GMHA in a mass ratio 3:2, preserving the overall concentration at 5% w/v. This was labeled HAGel ink. Finally, in both formulations, LAP was added as a photoinitiator (0.25% wt).

2.5. Rheological Evaluation

A comprehensive rheological analysis was conducted using an Anton Paar MCR 502 rheometer (Anton Paar GmbH, Austria) to evaluate the viscoelastic properties, temperature dependence, and shear-thinning behavior of the proposed polymer formulations (without photoinitiator) and assess their compatibility with extrusion-based printing process.

To identify the sol−gel transition temperature (T_g), temperature sweep tests were performed at a constant strain in the temperature range 4−37 °C, setting a heat-up ramp of 1 °C/min and an angular frequency of $\omega = 10\ s^{-1}$. The gelation temperatures of GelMA ($T_{g_{\mathrm{GelMA}}}$) and HAGel ($T_{g_{\mathrm{HAGel}}}$) were identified as the intersection point the storage modulus (G') and the loss modulus (G''). The linear viscoelastic (LVE) region was initially identified through an amplitude sweep test, set at $T_g$with a constant angular frequency ($\omega = 10\ s^{-1}$). Finally, frequency sweep tests were conducted at $T_g$with a constant strain below the LVE threshold to describe the viscoelastic behavior of the material in response to oscillatory mechanical stress.

To ascertain the gelation time of both formulations, time sweep tests were conducted at the strain limiting amplitude and constant angular frequency ($\omega = 10\ s^{-1}$) at T_g, with an analysis time of 3 h. The gelation times for both materials were determined at the point where the value of $G'$was equal to G''. Regarding the viscosity η of the two inks, rotational tests were conducted at $T_g$over a shear rate ($\dot{\gamma}$) range of 0.1−100 s^{-1}. In both cases, the viscosity values were reported as a function of $\dot{\gamma}$.

Finally, a three-interval rotational test was performed to simulate the extrusion printing conditions and to estimate the recovery kinetics of the ink. The first stage of the rotational test (i.e., the preshear phase) was conducted to simulate the behavior of the inks at rest (500 s, at $\dot{\gamma} = 0.01\ s^{-1}$). The second stage involved a rapid increase in shear stress ($\dot{\gamma} = 100\ s^{-1}$) over 5 s, which was intended to simulate the extrusion of the material through the nozzle. The third and final stage returned the system to the resting condition for 500 s to evaluate the shear-thinning property of the material and the time-dependent ability to recover the initial viscosity value.

Furthermore, rheological analyses were also conducted on samples after UV-induced crosslinking (1 min exposure) to enable a comparison of the viscoelastic properties of the hydrogel in its pre-crosslinked (extrusion) and post-crosslinked (stabilized network) states. An amplitude sweep test was first performed to determine the LVE region of the UV-crosslinked samples at room temperature using a constant angular frequency ($\omega = 10$ rad s^{-1}). Once the LVE was defined, frequency sweep measurements were carried out at a fixed strain of 0.1% to characterize the viscoelastic behavior of the material under oscillatory mechanical deformation.

2.6. Mechanical Characterization

The mechanical properties of the formulations were characterized by compression testing using a TA RSA III Dynamic Mechanical Analyzer equipped with a 35 N load cell. Cylindrical specimens with 1 cm diameter and 1 cm height were tested at a constant displacement rate of 0.1 mm/s.

Stress (σ) and strain (ε) were calculated from the recorded force (F), cross-sectional area (A_0), initial length (L_0), and displacement (ΔL) according to eqs 3 and 4:

$$\sigma = \frac{F}{A_0} \quad (3)$$

$$\varepsilon = \frac{\Delta L}{L_0} \quad (4)$$

The elastic modulus of the material was determined as the slope of the stress–strain curve in the strain range 0–0.05. Stress and strain at break were defined as the values corresponding to the point of sample failure, identified as the last measurable point before fracture-induced stress collapse.

2.7. Printability Assessment

2.7.1. Shape Fidelity Analysis. The BIO X 3D bioprinter (CELLINK, Sweden) was equipped with a cooling printhead and a 27G nozzle. The grid geometry (square base: 10 × 10 mm, thickness: 0.2 mm) with 2.25 mm pore sizes was specifically designed to simultaneously assess printing fidelity and provide a pore architecture that supports nutrient and oxygen transport under in vitro culture conditions.

Each ink was loaded into a 3 mL cartridge (CELLINK, Sweden), brought to the respective gelation temperatures for 30 min, and printed onto a print bed at 15 °C. The printed structures were then crosslinked

https://doi.org/10.1021/acsabm.6c00299
ACS Appl. Bio Mater. 2026, 9, 6370−6387

via UV photopolymerization (Alonefire UV torch, λ = 365 nm, power = 2400 mW/cm^2) for 30 s. According to the rheological characterizations, preliminary experiments were performed to assess the optimal range for a uniform filament deposition and a defined grid structure. The pressure was set in the range of 18−20 kPa, with a step variation of 1 kPa, while the printing speed was varied in the range of 4−8 mm/s, with a delta of 2 mm/s. A design of the experiment was defined according to these parameters, randomizing the structure fabrication. The scaffolds were 3D printed in triplicate for each condition. Representative images of the structures were collected from an overhead perspective, at the end of each printing, using the HD Camera tool head (CELLINK, Sweden). A customized Python code was used to binarize the images with a fixed threshold and subsequently extract the area and perimeter data of each individual pore. Pore squareness was calculated as described by eq 5:

$$\text{Pore squareness (PS)} = \frac{p^2}{16A} \tag{5}$$

where p and A are the perimeter and the area of the pores, respectively. PS values close to 1 were indicative of a square shape of the pore (according to the CAD model), while a round shape is correlated to an index value close to 0. A mean value for each image was obtained over the printed pores. The final average, representative of the scaffold type, was then calculated from the triplicates. As a parameter representative of the overall printability of the proposed formulations, the Scaffold Pore Fidelity Index (SPFI) was defined in accordance with our previous work[28] and calculated as reported in eq 6:

$$\text{Scaffold Pore Fidelity Index (SPFI)} = \frac{\sum_{i=1}^{K} A_i / A_{\text{nom}}}{K} \tag{6}$$

where A_i represents the effective area of the ith pore of the structure, A_{nom} is the nominal area of the pore in the CAD file, and the denominator K corresponds to the number of pores per structure (i.e., 16). In this way, we provided an evaluation of the structural accuracy of the 3D printed scaffold, with information on the extrusion and missing pores. Indeed, a value of the pore areas lower than the nominal ones could be indicative of an overextruded scaffold, whereas an SPFI > 1 refers to underextrusion conditions and/or missing pores. The implementation of the code for image analysis is based on an initial binarization step imposing a threshold of 250 followed by the definition of a region of interest (ROI), which was set to crop a subimage per pore region, in each grid (i.e., 16 subimages). The area of each pore was calculated and normalized to the nominal value as shown in the previous equation. SPFI was estimated for each scaffold, and the mean value was calculated by the triplicates. This approach was performed for each combination of printing parameters investigated. The values of the PS and SPFI parameters are reported in the form of a printability heat map utilizing both pressure and speed as regressor and incorporating their interactions up to the second order.

2.7.2. Scaffold Stability and Water Uptake. A four-layer grid (square base: 10 × 10 mm, height: 0.4 mm) was designed with the Autodesk Inventor software (Autodesk, San Rafael, CA) and used as representative 3D scaffold for the evaluation of the stability of a printed structure, the bioprinting, and the cell assays. Printing parameters were set according to the shape fidelity results to obtain well-resolved systems with geometric accuracy for both ink formulations. In detail, the printing velocity was kept constant at 6 mm/s, while pressure was set respectively at 20 kPa for GelMA and 18 kPa for HAGel. Following printing, the scaffolds were weighed and incubated in PBS up to 14 days at 37 °C, 5% CO_2. After 1, 3, 7, and 14 days, the structures were retrieved from the PBS solution, the excess of water was removed, and they were weighed to estimate the corresponding mass, labeled as wet weight (w_{wet}). At each time point, sacrificial structures were lyophilized and weighed, obtaining the corresponding mass value in dried state (w_{dry}). All measures were performed in triplicate. eqs 7 and 8 were used to calculate the mass loss (ML)[25,29] and the water uptake (WU)[30,31] of the printed systems, as follows:

$$\text{ML}\,[\,\%\,] = \frac{w_{\text{dry},0} - w_{\text{dry},t}}{w_{\text{dry},0}} \times 100 \tag{7}$$

$$\text{WU}\,[\,\%\,] = \frac{w_{\text{wet},t} - w_0}{w_0} \times 100 \tag{8}$$

In eq 7, the terms $w_{\text{dry},0}$ and $w_{\text{dry},t}$ indicate the weights of the freeze-dried construct at day 0 (i.e., postprinting) and at a chosen time point (i.e., t), respectively. In eq 8, $w_{\text{wet},t}$ is indicative of the hydrated scaffold weight at the target time point, and w_0 corresponds to the scaffold weighted immediately after the printing process.

2.8. Cell Culture

The human ovarian serous adenocarcinoma cell lines SKOV3 (ATCC HTB-77) and OVCAR3 (ATCC HTB-161) were obtained from the American Type Culture Collection (LGC Standards, Teddington, UK). KURAMOCHI cells were provided by the National Institutes of Biomedical Innovation, Health, and Nutrition (NIBIOHM). SKOV3 cells were maintained in McCoy's 5A medium (cat. #26600-023, GIBCO Thermo Fisher), while OVCAR3 and KURAMOCHI cells were cultured in RPMI-1640 medium (cat. #618700-010, GIBCO Thermo Fisher).

The OVCAR3 medium was supplemented with 20% FBS (cat. #A5256701, Gibco), whereas the other media contained 10% FBS.

All media were additionally supplemented with 100 U/mL penicillin and 100 μg/mL streptomycin. Cells were incubated at 37 °C in a humidified atmosphere containing 5% CO_2 and split every 4 days to avoid significant confluence phenomena.

2.9. 3D Bioprinting

The printing process of the cell-laden ink (i.e., GelMA and HAGel) was performed as follows. Lyophilized polymers were exposed to UV light for 1 h for sterilization purposes, ensuring the preservation of methacrylate functionality (Supporting Information Figure S3); then, the polymer was dissolved in PBS under sterile conditions according to the amounts discussed in Section 2.4. The photoinitiator solution was sterilized by filtration (0.22 μm sterile filter) and subsequently added to the polymer solution. Each cell line was separately embedded in GelMA and HAGel to evaluate the behavior of the cell type in the specific polymer matrix. Cells were trypsinized, pelleted, resuspended in 50 μL, and added to the ink formulation to obtain a final concentration of 6 × 10^6 cells/mL. The cell-laden ink was then loaded into a 3 mL cartridge equipped with 27G nozzle and hosted into the temperature-controlled printhead to achieve the desired printing temperature (i.e., 20 °C for GelMA and 18 °C for HAGel). The resulting constructs (square base: 10 × 10 mm; height 0.4 mm) were exposed to UV light (λ = 365 nm, for 1 min, distance lens−construct: 9 cm), submerged in fresh cell culture medium according to the used OC cell line, and incubated at 37 °C, 5% CO_2 up to 14 days. Three independent experiments were performed per cell line.

2.10. Confocal Imaging and In Vitro Cell Assays

2.10.1. Cell Viability. Cell viability into the printed structures was quantified by means of a live and dead (L/D) assay 1, 3, 7, and 14 days postprinting. The staining solution was prepared by adding Calcein AM (1.25 μL/mL) and EthD-1 (2 μL/mL) in fresh medium and, after the withdrawal of the incubating medium, administered to each construct for 1 h at 37 °C, 5% CO_2. The 512 × 512 pixel live cell images were acquired through a confocal microscope (Fluoview FV10i, Olympus Life Science, England) equipped with an integrated incubator, four diode lasers (wavelengths: 405, 473, 559, and 635 nm), and a 10 × phase-contrast objective (0.4 NA). The pinhole size was set to 1 Airy unit. Z-stack images were acquired at 5 μm steps over a height of 200 μm for each construct at a resolution of 2.49 μm/pixel. Live cells stained with Calcein-AM were imaged with excitation at λ = 488 nm and emission collected in the 490–540 nm range (green channel), while dead cells

https://doi.org/10.1021/acsabm.6c00299
ACS Appl. Bio Mater. 2026, 9, 6370−6387

stained with EthD-1 were imaged with excitation at λ = 559 nm and emission collected in the 570–620 nm range (red channel). To ensure a representative analysis, three distinct regions of each scaffold were imaged: two corresponding to filament intersections and one situated at the outer edge of the construct (Supporting Information Figure S1).

For each scaffold composition and investigated time point, three independent experiments were performed. The analysis was conducted using the ImageJ/Fiji software on five equally spaced images extracted from the *z*-stack. Cell viability was calculated as the ratio of viable cells (counted from green channel images) to the total number of cells (obtained by summing viable and nonviable cells detected in the green and red channels, respectively) according to eq 9:

$$\text{Cell viability } [\,\%\,] = \frac{N_{\text{live}}}{N_{\text{live}} + N_{\text{dead}}} \times 100 \tag{9}$$

where N_{live} and N_{dead} are the number of live and dead cells, respectively. The estimation of the cell density (i.e., total number of cells per unit area of scaffold) was also performed: the scaffold mean area ($\overline{A}$) was calculated from the *z*-stacking of the acquired slices (ImageJ/Fiji software: max intensity *Z*-projection) and used as reference area for the estimation of cell density. For each time point, cell counting was carried out by analyzing the selected scaffold regions (i.e., the aforementioned two junctions and one border) across five different planes within the *z*-stack. The cell density index (CDI, eq 10) was calculated by dividing the number of counted cells in each plane ($N_{\text{live}} + N_{\text{dead}}$) by $\overline{A}$ and normalizing with respect to the corresponding layer cell density at day 1 ($\text{CD}_{\text{cell},1}$).

$$\text{CDI} = \frac{\text{CD}_{\text{cell},t}}{\text{CD}_{\text{cell},1}} \tag{10}$$

where

$$\text{CD}_{\text{cell},t} = \frac{(N_{\text{live}} + N_{\text{dead}})_t}{\overline{A}} \tag{10.1}$$

and

$$\text{CD}_{\text{cell},1} = \frac{(N_{\text{live}} + N_{\text{dead}})_1}{\overline{A}} \tag{10.2}$$

The subscripts *t* and 1 are indicative of the investigated time point, i.e., day *t* (3, 7, and 14) and day 1, respectively.

2.10.2. Immunostaining. Cell morphology, spatial organization, and proliferation were evaluated into the 3D printed structures. At the desired time point, the constructs were washed in PBS and fixed for 1 h in 4% paraformaldehyde. After washing three times with PBS, 0.25% Triton X-100 in PBS was added for 1 h to permeabilize the fixed constructs. Samples were then incubated at RT for 45 min with phalloidin-TRITC (1:200, in 2% BSA + 0.1% Triton X-100 in PBS), and after a rinsing step with PBS, cell nuclei were stained with 15 min incubation of Hoechst 33342 (1:500, in 2% BSA + 0.1% Triton X-100 in PBS). *Z*-stack images at 2 μm steps were acquired at 60× magnification using a confocal laser scanning microscope (Fluoview FV10i, Olympus Life Science, England) at a resolution 1024 × 1024 pixels (0.2071 μm/pixel) for each condition. F-actin were imaged in the red channel (excitation 559 nm, emission 570−620 nm) and cell nuclei in the blue channel (excitation 358 nm, emission 440−480 nm).

2.11. RNA Isolation and qRT-PCR

Bioprinted constructs containing HG-SOC were treated with 1.5% type II collagenase prepared in TES buffer and incubated at 37 °C for 1 h in 100 μL of solution. After complete digestion, the samples were centrifuged at 8000 rpm for 5 min at 4 °C to pellet the cells. The supernatant was discarded, and the cell pellets were resuspended in cold PBS. Three washes were performed prior to RNA extraction using PureZol (cat. #7326880, Bio-Rad Laboratories, Italy) according to the manufacturer's instructions, and 1 μg was used for retrotranscription (RT) using the PrimeScript RT Reagent Kit (cat. #RR037A, Takara).Quantitative real-time PCR was performed by using the light Cycler QuantStudio 3 qPCR System (Applied Biosystem) using the SensiFAST SYBR Hi-ROX One-Step Kit (Meridian Bioscience). Final data were obtained by using the $2^{-\Delta\Delta Ct}$ method. The number of each gene-amplified product was normalized to the number of GAPDH amplified products. The primers (PrimeTime qPCR primers from IDT) used were as follows:

CD44
Primer F: 5'-GATCACCGACAGCACAGAC-3'
Primer R: 5'-TTCGTCCACCTTCTTGACTC-3'
ICAM1
Primer F: 5'-GCTATTCAAACTGCCCTGATG-3'
Primer R: 5'-GCGTAGGGTAAGGTTCTTGC-3'
HMMR
Primer F: 5'-GATACTACCTTGCCTGCTTA-3'
Primer R: 5'-GCTTCCATCTTTCCAACTCAG-3'
MMP14
Primer F: 5'-TTCGCCGACTAAGCAGAAG-3'
Primer R: 5'-CTTGAATTCCTAGACCGCTGT-3'
MMP2
Primer F: 5'-TCCACCACCTACAACTITGAG-3'
Primer R: 5'-GTGCAGCTGTCATAGGATGT-3'
GAPDH
Primer F: 5'-ACATCGCTCAGACACCATG-3'
Primer R: 5'-TGTAGTTGAGGTCAATGAAGGGG-3'

2.12. Western Blotting (WB)

For WB analysis, total cells were detached by scraping, collected by centrifugation, and lysed in RIPA buffer [50 mM Tris·HCl (pH 7.5), 150 mM NaCl, 1% Nonidet P-40, 0.5% sodium deoxycholate (NaDoc), and 0.1% SDS] containing proteases and phosphatase inhibitors (cat. #5872, Cell Signaling). Protein concentrations were determined using the DC Protein assay (cat. #5000115, Bio-Rad Laboratories, Italy). Cell lysates were resolved on 10% Mini-PROTEAN TGX Precast Protein Gels (cat. #4561034, Bio-Rad Laboratories, Italy), transferred to nitrocellulose membranes (Bio-Rad Laboratories, Italy) followed by WB with indicated primary antibodies, and revealed by using goat Anti-Rabbit IgG (H + L)-HRP Conjugate (cat. #1706515, Bio-Rad Laboratories) and goat Anti-Mouse IgG (H + L)-HRP Conjugate (cat. #1706516, Bio-Rad Laboratories, Italy). Proteins were visualized by chemiluminescence (cat. #1705061, Clarity Western ECL Substrates, Bio-Rad Laboratories, Italy) by using Azure 300 (Azure Biosystems, USA). Quantification analyses were performed using ImageJ and reflected the relative amounts as a ratio of each protein band relative to the loading control of the lane. Antibodies (Abs) used were the CD44 Polyclonal antibody (cat. #15675-1-AP, Proteintech, UK) and GAPDH (cat. #G945, Merck, Germany).

2.13. Statistical Analysis

Data were analyzed using Prism ver. 10.4.1 (GraphPad Software, San Diego, CA) and reported as mean ± SD if not otherwise specified. The statistical significance was set at the 0.05 level and evaluated through one-way analysis of variance (one-way ANOVA) followed by Tukey's multiple-comparison test or two-way ANOVA.

3. RESULTS AND DISCUSSIONS

3.1. Gel and HA Methacrylate Modification

We grafted methacrylic groups on the polymer backbones to obtain a chemically crosslinked scaffold, which enabled structural integrity over time. In particular, the methacrylation process involved the reaction between the methacryloyl and amine groups for Gel functionalization and the ring-opening in GMA mediated by the hydroxyl groups of HA.[32]

^{1}H NMR analyses were performed to validate the polymer modification, as reported in Figure 1. Referring to GelMA (Figure 1a),

https://doi.org/10.1021/acsabm.6c00299
ACS Appl. Bio Mater. 2026, 9, 6370−6387

the characteristic peaks at 5.63 and 5.41 ppm correspond to acrylic protons of methacrylamide groups, which are not detectable in the neat gelatin. Additionally, the attenuation of the signal related to the lysin methylene (2.9 ppm) in the GelMA vs Gel spectrum further demonstrates the reaction of the gelatin amine groups with MA. Setting the phenylalanine peak as internal reference, the comparison of these integral values can lead to the estimation of the DoF according to eq 1, which was equal to ca. 50 %.

Referring to GMHA, the acrylate group was conjugated to the HA chain through either an epoxide ring-opening reaction or a reversible transesterification through the hydroxyl group.[26,33] The polymer functionalization was confirmed by the methacrylate peaks at 6.1, 5.6, and 1.8 ppm (Figure 1c). The percentage of methacrylation can be calculated from the relative integral values of the methacrylate protons and methyl protons in HA acetamide group, which resulted in ca. 21%.

Further confirmation of methacryloyl modification of Gel and methacrylate modification of HA was provided by IR spectroscopy (Supporting Information Figure S2). Specifically, the comparison between Gel and GelMA spectra highlighted the C═O stretching at 1638 cm^{-1} of the amidic linkage MA-Gel, whereas the characteristic signals of the gelatin structure were detectable in both spectra, such as the −OH stretching (at 3283 cm^{-1}), N−H stretching (at 3066 cm^{-1}), and C−H stretching (at 2934 cm^{-1}). Regarding HA, the distinctive −OH stretching is visible at 3500−3150 cm^{-1}, while the bands at 2965 and 2815 cm^{-1} correspond to the symmetric and asymmetric C−H stretching. The signals at 1615, 1560, and 1312 cm^{-1} are ascribable to the amide II C═O stretching, N−H bending, and amide III, respectively. Confirmation of the methacrylation of HA is provided by the presence of a peak at 1701 cm^{-1}, ascribable to the C═C stretching, and an increased intensity in the shoulder peak at 1655 cm^{-1}, which corresponds to the ester C═O stretching of the formed bond.

The preservation of methacrylate functionalities was further confirmed after UV-based sterilization procedure applied to the lyophilized polymers for subsequent sterile 3D printing, suggesting that UV exposure of the solid polymers, in the absence of photoinitiator, does not compromise the photocrosslinkable groups (Supporting Information Figure S3).

3.2. Polymer Ink Formulation and Rheological Characterization

The ink formulations were designed using a fixed total polymer concentration of 5% w/v, selected as a well-established working range for gelatin-based systems in extrusion 3D printing.[34−36] Within this fixed concentration, compositional tuning was performed by introducing GMHA in the hybrid formulation (i.e., HAGel), maintaining GelMA as the reference component. This design allowed the direct evaluation of the effect of HA incorporation on the rheological and biological properties of the system without altering the overall polymer content.

The rheological properties of the polymer solutions were characterized to assess their feasibility for 3D printing. To estimate the optimal printing temperature, the T_g of the polymer solutions was

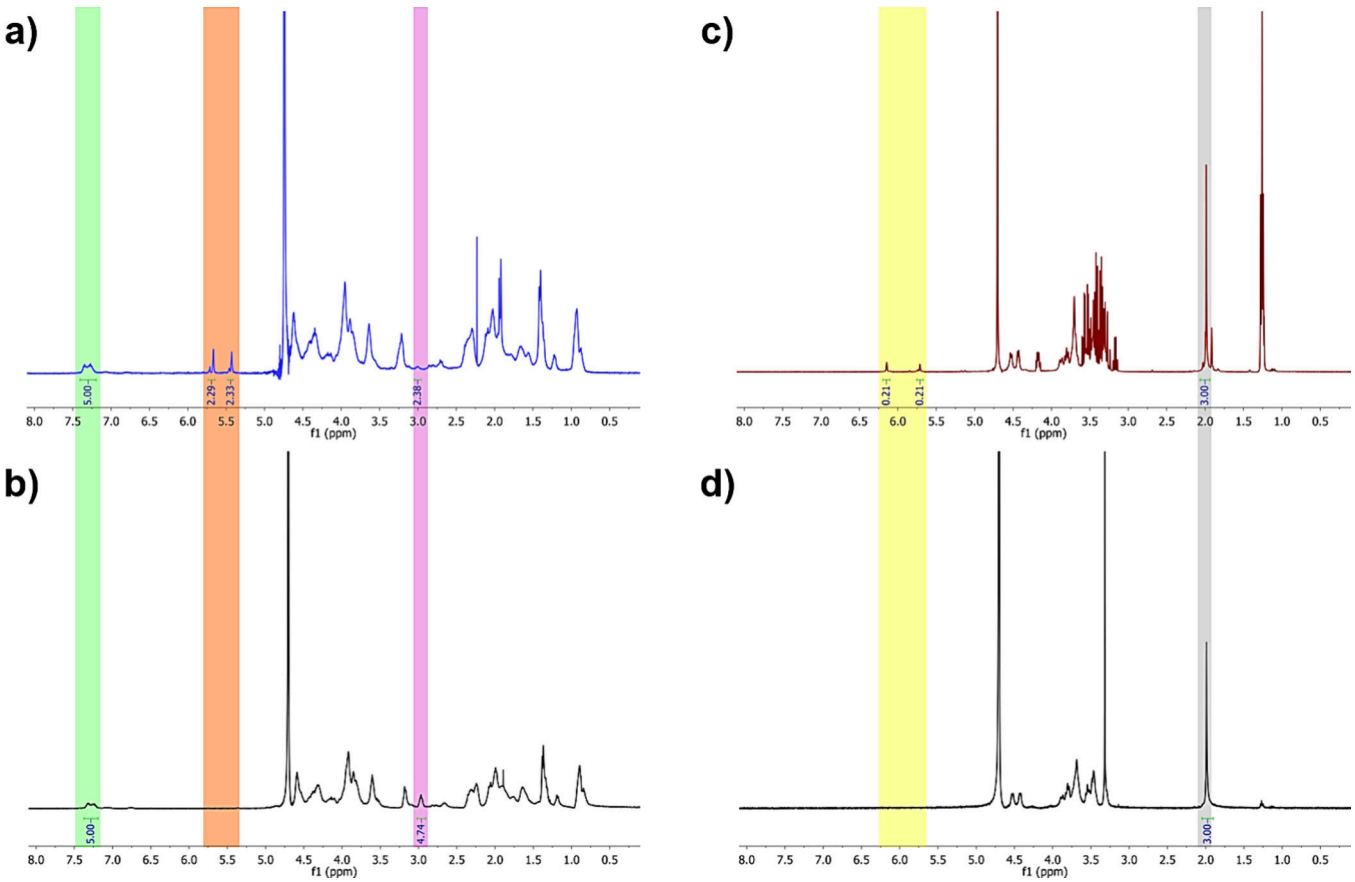

Figure 1. ^{1}HNMR spectra of GelMA (a), Gel (b), GMHA (c), and HA (d). The characteristic peaks of the functionalization and for the estimation of the DoF are highlighted with colored bands. For GelMA and Gel: phenylalanine aromatic moieties (green), vinyl groups (orange), and lysine methylene protons (pink). For GMHA and HA: methacrylate groups (yellow) and methyl protons (gray).

https://doi.org/10.1021/acsabm.6c00299
ACS Appl. Bio Mater. 2026, 9, 6370−6387

evaluated through temperature-dependent measurements (i.e., cool down ramp) of G' and G'', as reported in Figure 2a. Upon the onset of gelation, the material began to exhibit a marked elastic response, with a sudden increase in G' relative to the value before gel formation. The crossover point (i.e., $G' = G''$) indicative of the liquid-to-gel transformation was observed at 21 °C for GelMA and 18 °C for HAGel followed by a rapid increase in G' values. The rapidity of the transition is corroborated by the results of the time sweep test (Figure 2d), which indicated a gelation time of ca. 70 s for GelMA and ca. 115 s for HAGel.

Amplitude sweep tests provided insight into the viscoelastic behavior of both inks at their respective T_g. As shown in Figure 2b, the trends of G' and G'' as a function of shear strain confirm a gel-like state for both formulations (i.e., $G' > G''$), with an LVE region up to 0.2% and 0.15% for GelMA and HAGel, respectively. The limiting strain amplitude for LVE response was therefore identified as $\gamma = 0.1\%$ to accommodate both inks. Furthermore, the yield stress (τ_y) was determined as the maximum shear stress within the LVE region, and the flow (τ_f) point was identified at the intersection where G' equals G''. τ_y and τ_f were equal to 67.5 and 24.2 Pa, respectively, for GelMA and 10.4 Pa and 6.3 Pa for HAGel. The presence of the HA component, due to its high hydrophilicity, interferes with the intermolecular interactions of GelMA, facilitating the transition to the nonlinear regime and reducing flow resistance, ultimately leading to a lower flow point.[37]

Referring to the frequency sweep graphs (Figure 2c), the elastic component dominated the viscoelastic behavior, ($G' > G''$), indicating high structural stability. Furthermore, both inks did not exhibit a fluid or viscous behavior, as the storage modulus was greater than the loss modulus and both are almost independent of the frequency.

The comparison of viscosity profiles of the two inks as a function of shear rate is shown in the Figure 2e. Throughout the entire analysis range, the viscosity of the HAGel remained lower than GelMA, achieving a similar value at high shear rate values (100 s^{-1}) only. Overall, the presence of GMHA influences the viscous properties of the ink even at low shear rates (0.1 s^{-1}). This can be attributed to the distinct molecular properties of HA, characterized by its linear backbone, which reduces polymer chain entanglements, thereby decreasing flow resistance compared to the GelMA formulation.

Finally, the analysis of the recovery kinetics demonstrates that both samples enabled an almost complete recovery of the initial viscosity value following the abrupt change in shear rate applied over a short period. The recovery time for both inks is approximately 75 s (Figure 2f).

The characterization of the crosslinked hydrogels was also performed to provide a comprehensive overview of the viscoelastic properties of the final constructs following 3D printing and UV-induced photocrosslinking. The results of the amplitude sweep and frequency sweep tests are reported in Figure 3. As shown in Figure 3a, both formulations exhibited a predominant elastic behavior after UV exposure, maintaining a gel-like state with G' consistently higher than G'' over the investigated strain range. In addition, the increase in storage moduli compared to the precrosslinked samples was consistent with a successful photocrosslinking and network stabilization. The LVE region also extended toward higher strain values, reaching 19.4% and 37.5% for GelMA and HAGel hydrogels, respectively. Results from the frequency sweep test (Figure 3b) showed a nearly constant trend of G' over G'', further confirming the structural stability of the crosslinked network. Although GMHA exhibited a lower degree of methacrylation compared to GelMA, the incorporation of HA may have contributed to increased network organization through both physical chain entanglement and the participation of additional methacrylate groups in the photocrosslinking process. Moreover, the hydrophilic and extended conformation of HA chains in solution could improve the accessibility and distribution of reactive groups within the polymer network, ultimately contributing to the enhanced viscoelastic stiffness observed in the HAGel system.[38] Compression analyses further supported these findings. As shown in Figure 3c, the elastic modulus for the GelMA hydrogel was 7.9 kPa and that for the HAGel specimen was equal to 33.1 kPa, whereas the strain at break decreased from 0.76 for GelMA to 0.37 for HAGel.

These results indicate that the incorporation of GMHA promoted the formation of a stiffer network, although the lower strain at break suggests a reduced deformability and a more brittle behavior. This may be attributed to the increased network constraints and reduced polymer chain mobility mediated by HA motifs.[39]

3.3. Printability Assessment

The printability maps of PS and SPFI for GelMA and HAGel were derived from the multivariate ordinary least squares (OLS) regression.[28] As illustrated in Figure 4a, the PS values for both inks remained almost constant within the defined printing parameters, suggesting that the pore geometry is not significantly affected in this range of values. However, PS did not consider the overall number of pores and, hence, the fidelity with the nominal design. The maps for SPFI validated the effect of the extrusion pressure (P) and velocity (v) on the outcome. The optimal value for SPFI is equal to 1, representing a scenario where the calculated area perfectly overlaps with the ideal area. Deviations from this value correspond to underextrusion (SPFI > 1) or overextrusion (SPFI < 1). Here, the printing feasibility of GelMA and HAGel was different. GelMA exhibited a broader range of conditions eligible for achieving structures as expected from nominal CAD. The optimal combination of parameters was identified as $P = 20$ kPa and $v = 6$ mm/s. Regarding HAGel, the distribution of optimal parameters was narrower, highlighting optimal printability at low pressure and low velocity, i.e., 18 kPa and 6 mm/s. Overextrusion failure occurs at high pressure and low speed settings (Figure 4b).

3.4. Stability of the Printed Scaffolds

The water uptake (WU) and degradation of hydrogel-based constructs depend on various factors, including pore size, crosslinking density, and polymer−polymer and polymer−solvent interactions. The estimation of these properties plays a crucial role in the printing of cell-laden constructs, as they influence the ability to absorb fluids and regulate the diffusion of nutrients.[40]

Figure 5 illustrates the WU behavior of the printed GelMA and HAGel constructs. The GelMA formulation showed a fast weight increase within the first 7 days, reaching +36% w/w compared to day 0 (i.e., postprinting). After this time point, the percentage of WU decreased and stabilized around +13%, suggesting that the hydrogel may have reached a hydrated equilibrium state, potentially accompanied by the onset of slight structural degradation (as further discussed in the next paragraph). On the other side, the WU values for HAGel were similar at all investigated time points (ranging between +6 and 10%), indicating no significant variations in the polymer chain solvation following the 3D printing. This difference can be attributed to the diverse polymer composition

https://doi.org/10.1021/acsabm.6c00299
ACS Appl. Bio Mater. 2026, 9, 6370−6387

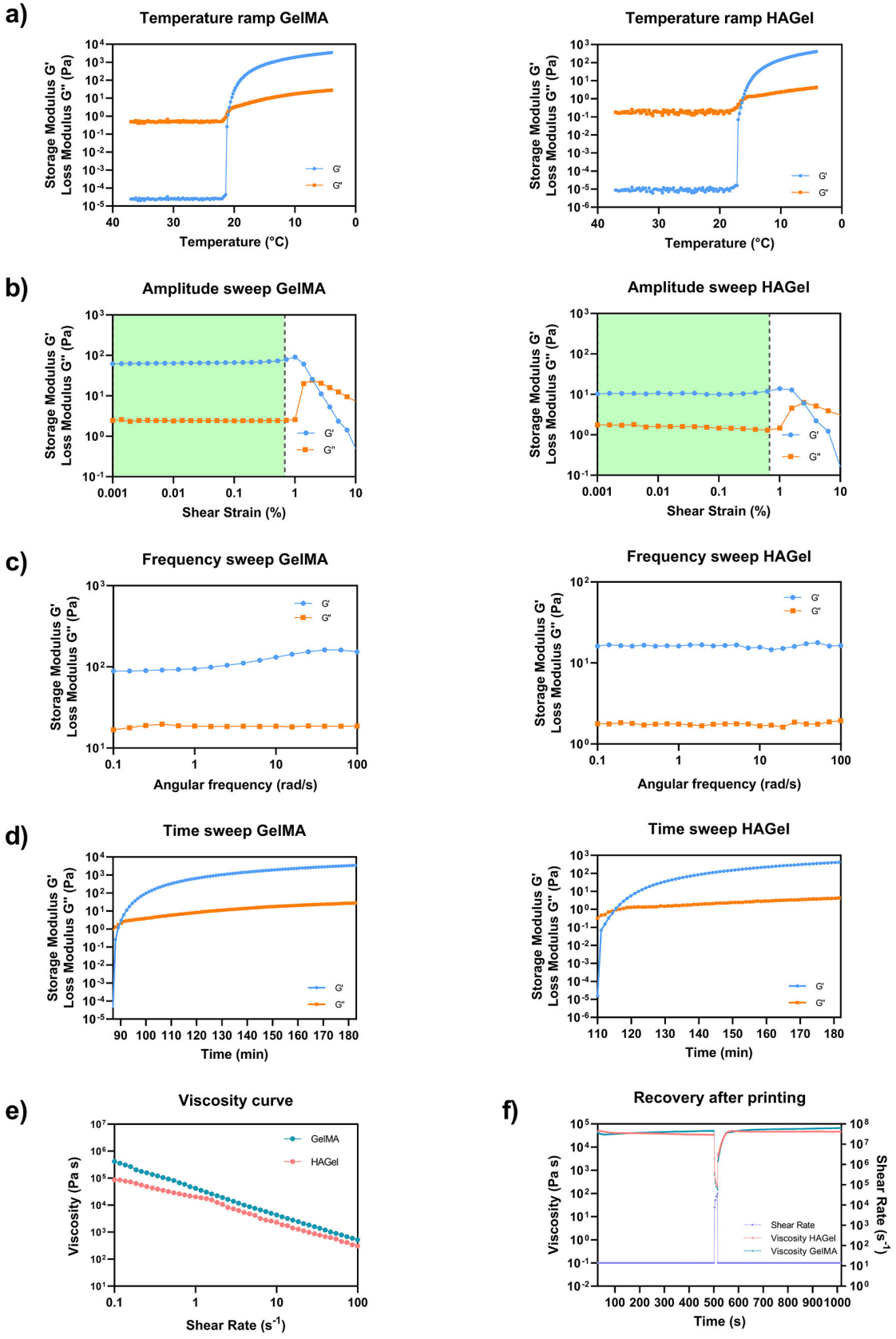

Figure 2. Rheological evaluation of the inks GelMA and HAGel. Temperature ramp test (a): storage and loss moduli as a function of temperature. Amplitude sweep test results: storage and loss moduli as a function of shear strain at the respective T_g of GelMA and HAGel. The green box highlights the LVE region, and the black dotted line shows the critical strain (b). Frequency sweep test results: storage and loss moduli as a function of angular frequency (c). Time sweep test: storage and loss moduli as a function of time (d). Viscosity curve (e): comparison between GelMA and HAGel. Recovery kinetics of the inks (f): viscosity as a function of time with three intervals of applied shear strain.

https://doi.org/10.1021/acsabm.6c00299
ACS Appl. Bio Mater. 2026, 9, 6370−6387

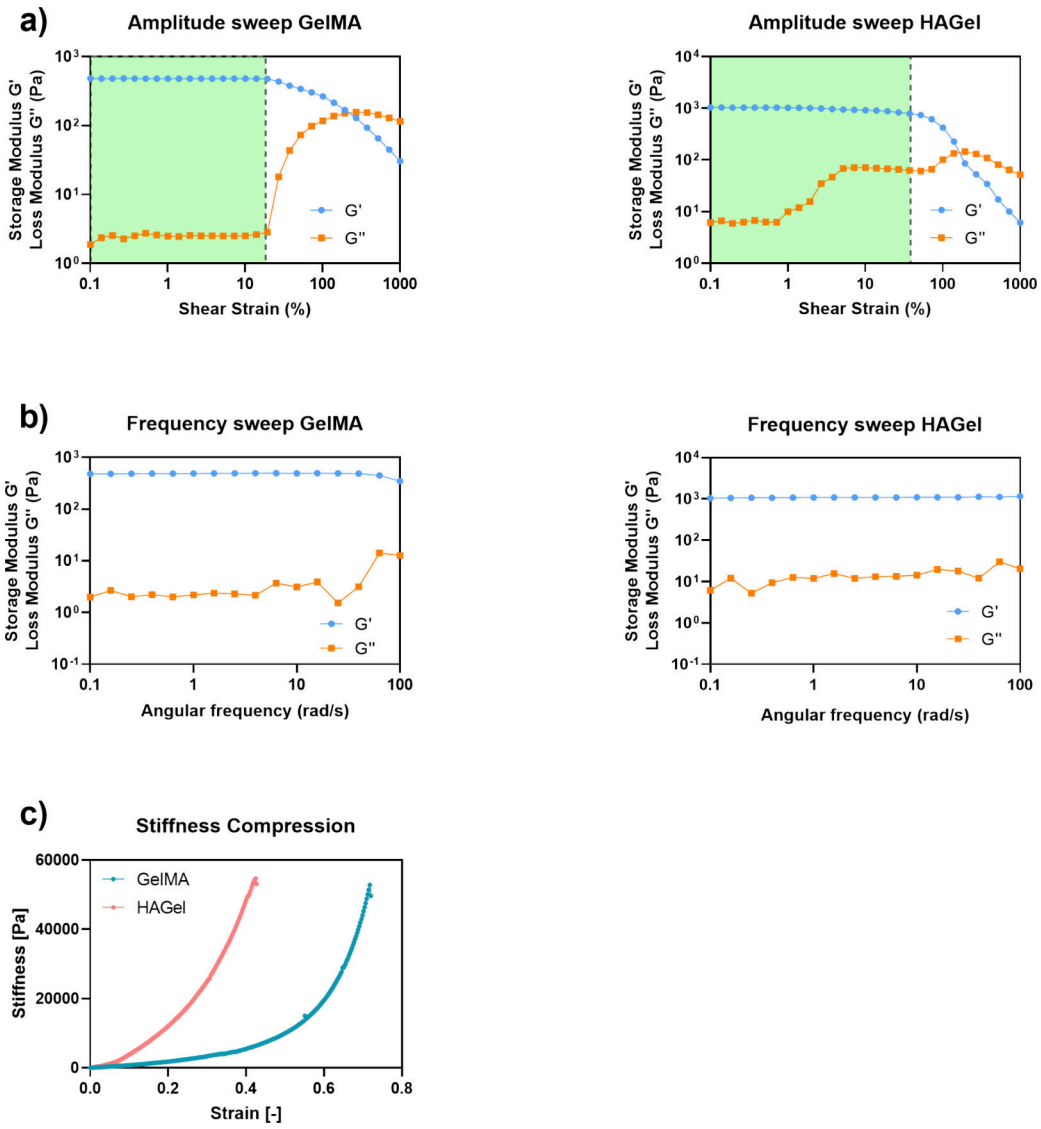

Figure 3. Rheological and mechanical evaluation of crosslinked GelMA and HAGel inks. Amplitude sweep test results (a): storage and loss moduli as a function of shear strain of GelMA and HAGel. The green box highlights the LVE region, and the black dotted line shows the critical strain. Frequency sweep test results (b): storage and loss moduli as a function of angular frequency. (c) Compression load curves of GelMA and HAGel.

and intermolecular interactions. GelMA, as a single-component system, likely forms a more homogeneous network with a crosslinking density modulated by the steric hindrance of the gelatin backbone, enabling great water absorption.[41] In contrast, HAGel introduces network heterogeneity arising from the incorporation of GMHA with GelMA network. This results in differences in chain rigidity and polymer−polymer interactions, leading to an overall reinforcement of the hydrogel structure,[42] as evidenced by the increased viscoelastic and mechanical properties. Although HA is intrinsically hydrophilic, in this system, GMHA is covalently integrated into the crosslinked network and does not behave as a free hydrophilic component. Instead, its incorporation likely contributes to network connectivity through methacrylate-mediated crosslinking points and may enhance the physical interactions with gelatin counterpart (e.g., hydrogen bonds), affecting the free-chain extension in aqueous environment.[42,43]

Moreover, given the hydrogel-based nature of both scaffold formulations, the system wettability is intrinsically governed by their high water content and equilibrium-swollen state, which ensure a permanently hydrated interface under physiological conditions and a high surface wettability, collectively reflecting the polymer affinity for aqueous environments (Supporting Information Videos S1 and S2).

Regarding ML, consistent trends were observed over time for both GelMA and HAGel. After the first day, a mass loss of 15% was recorded for GelMA compared to HAGel, which exhibited a 5% decrease only. In the subsequent days, no further ML increase in GelMA was noticed (15.6% at day 14). These results can be probably explained considering both the release of uncrosslinked chains after the printing process in the first hours and the intermolecular interactions occurring in the two scaffolds, with extensive HA-Gel physical bonding contributing to the network stabilization.[44]

3.5. Cell Viability, Proliferation and Morphology Evaluation

Cell viability was assessed through a L/D assay, and representative confocal micrographs were collected at 1, 3, 7, and 14 days after bioprinting. The corresponding results are shown in Figure 6.

https://doi.org/10.1021/acsabm.6c00299
ACS Appl. Bio Mater. 2026, 9, 6370−6387

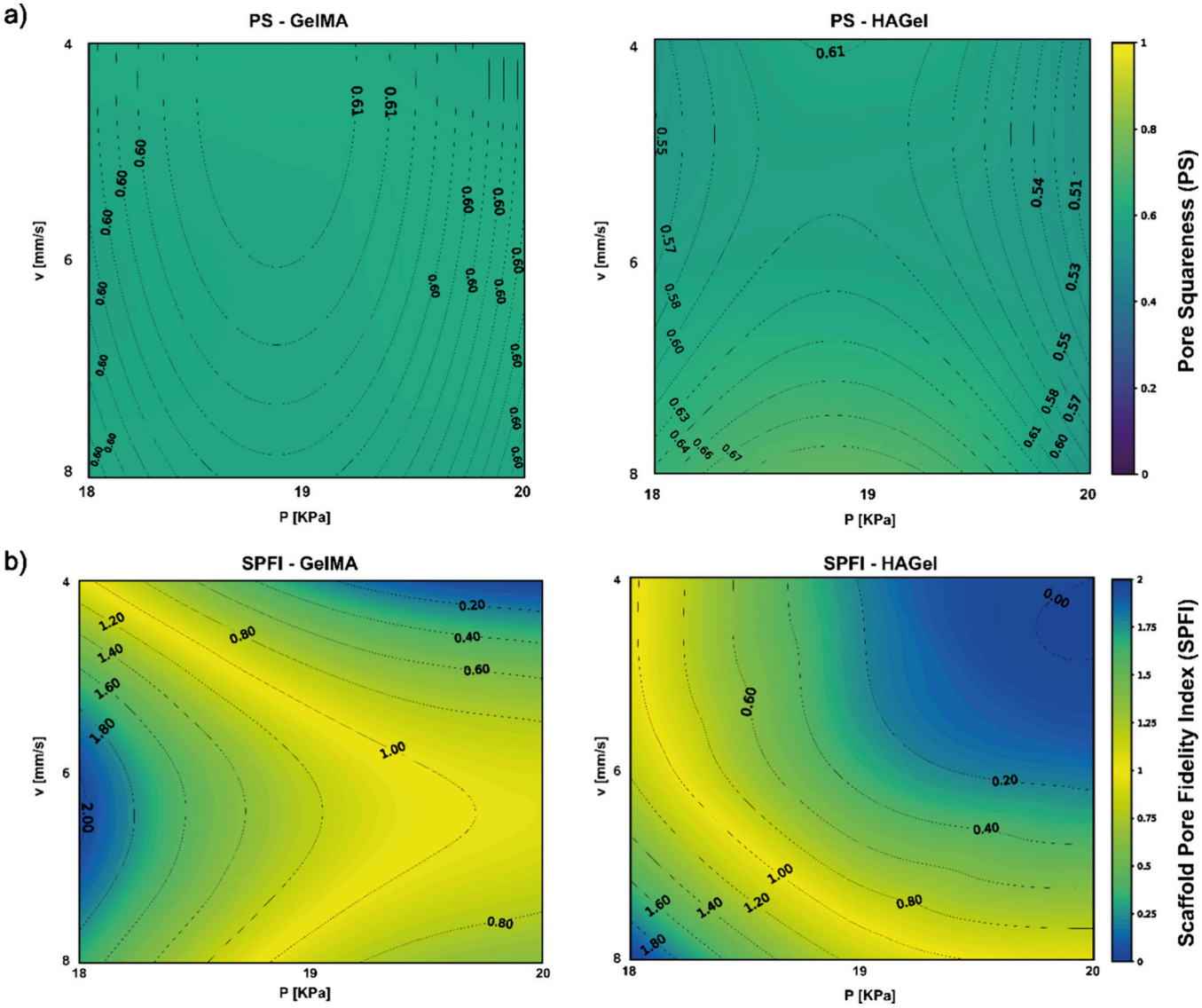

Figure 4. Printability evaluation of the inks GelMA and HAGel. Heat maps of PS (a) and SPFI (b): ink behavior as a function of the printing parameters pressure and velocity.

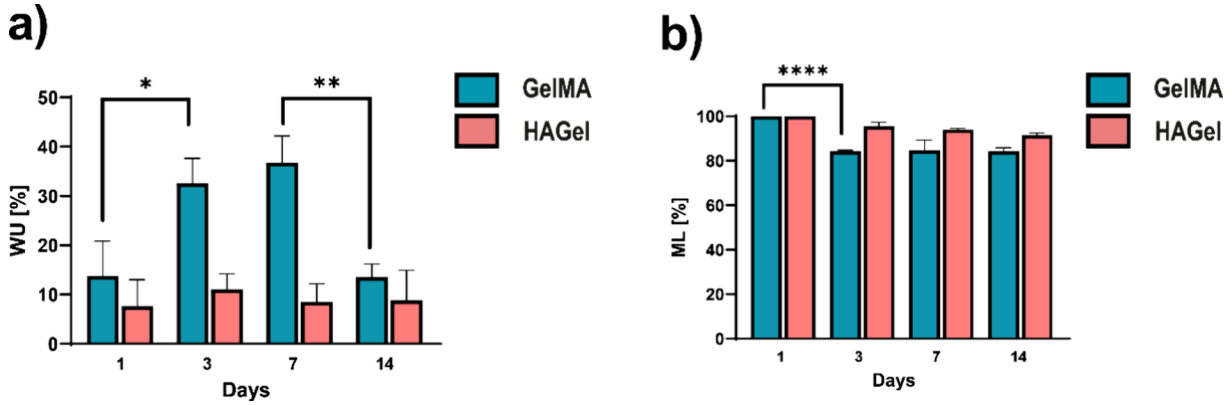

Figure 5. Water uptake (a) and mass loss (b) profile comparison between GelMA (petrol green) and HAGel (orange) up to 14 days. Statistical analysis was performed via one-way ANOVA for each formulation. *$p < 0.05$, **$p < 0.01$, ***$p < 0.001$, ****$p < 0.0001$, ns = not significant.

https://doi.org/10.1021/acsabm.6c00299
ACS Appl. Bio Mater. 2026, 9, 6370−6387

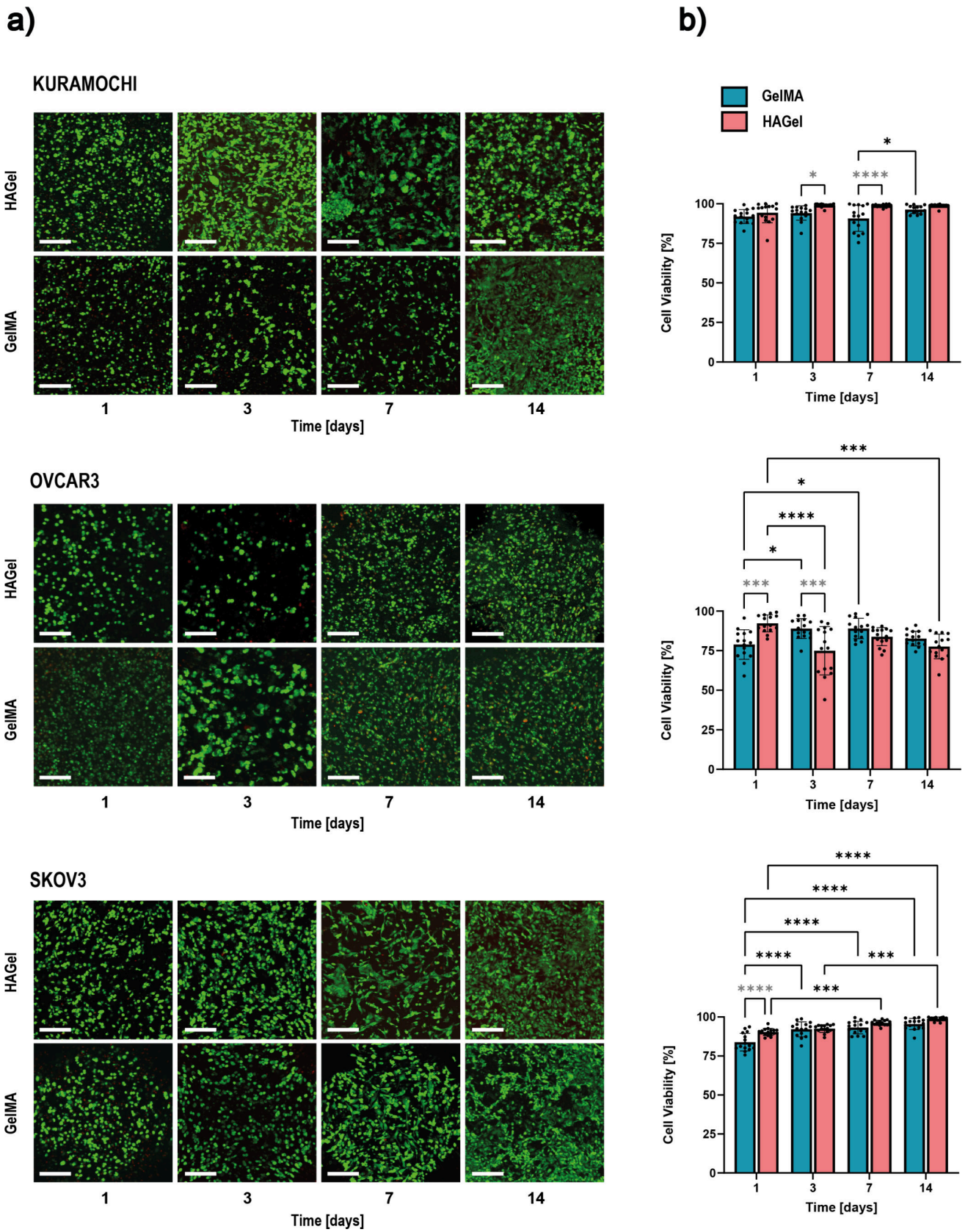

Figure 6. Cell viability within GelMA (petrol green) and HAGel (orange) scaffolds over time. (a) Representative maximum intensity *z*-projection images of the Live/Dead assay at days 1, 3, 7, and 14. Calcein-AM-positive cells are stained in green (live); EthD-1-positive cells are stained in red (dead). Scale bar 200 μm. (b) Analysis of cell viability (as a percentage of live cells with respect to the total number of cells). Reported statistical results refer to two-way ANOVA. Significance at fixed time points is highlighted in gray, whereas significance between the two formulations is reported in black. Significance levels are indicated as follows: $*p < 0.05$, $**p < 0.01$, $***p < 0.001$, $****p < 0.0001$.

https://doi.org/10.1021/acsabm.6c00299
ACS Appl. Bio Mater. 2026, 9, 6370−6387

Excellent viability results were obtained for the investigated conditions. KURAMOCHI cells showed high viability in both scaffolds. In GelMA, viability remained consistently around 88–94% throughout the incubation period, whereas in HAGel, it stabilized at higher values, reaching approximately 99% from day 3 onward. Notably, cell survival was significantly higher in HAGel compared to GelMA at day 3 ($p < 0.05$) and day 7 ($p < 0.0001$). This suggests a potential influence of HA within the polymer matrix on the overall cell culture.

Different trends were observed for OVCAR3 cells. With the exception of day 1 (where the lower viability may be attributed to the extrusion process), cell viability was generally higher in GelMA than in HAGel from day 3 onward (day 3: $p < 0.001$). In the HAGel-based cultures, a gradual decrease in viability was evident over the course of experiments (days 1–14: $p < 0.001$), suggesting that these cells were behaving in a distinct manner compared to KURAMOCHI cells.

For SKOV3, we noticed an increasing trend in cell viability during culture time for both hydrogel formulations, with a slightly higher mean viability in the HAGel formulation (differences are detectable at day 1: $p < 0.0001$).

We can infer that the printing process has an influence on the starting viability data, as extrusion-based bioprinting is known to impact cells depending on printing parameters and conditions.[45] Nevertheless, after 3 days of culture, adhered cells continued to grow within the construct, achieving optimal viability.

Cell density in printed scaffolds was evaluated through cell counting based on acquired images at the defined time points and normalized with respect to the total number of cells in the construct postprinting, at day 1. This analysis was conducted to estimate the impact of the polymer matrix composition on cell density across the area and, indirectly, the cell spreading/proliferation.

According to cell viability, KURAMOCHI cells were characterized by an increased cell number in HAGel vs GelMA, as confirmed by the cell density index at day 14 ($p < 0.05$). On the other hand, OVCAR3 cell density was higher in GelMA compared to HAGel, consistent with the viability data (at day 7 $p < 0.0001$ and at day 14 $p < 0.001$). SKOV3 showed a similar trend during culture time for the investigated substrates, with an increased cell density reached only at day 14 in the presence of HAGel ($p < 0.001$, Figure 7a). All cells displayed a decrease in cell count at day 3, which could be ascribed to a delayed effect of the extrusion process. Additionally, cells printed in both GelMA and HAGel exhibited proliferative activity, as confirmed by Ki67 staining (Supporting Information Figure S4) at 14 days postprinting. Results of F-actin immunostaining are presented in Figure 7b. KURAMOCHI, OVCAR3, and SKOV3 gradually acquired and sustained distinctive morphological features over the culture period,[46−48] with a noticeable increase in cell adhesion and spreading compared to day 1 when cells exhibited a rounded, dot-like appearance. This morphological progression was observed in both GelMA and HAGel matrices across all tested cell lines. Specifically, KURAMOCHI cells displayed a uniform and organized distribution over the polymeric substrate, forming a cohesive cellular epithelial sheet from day 7 onward. On the other side, OVCAR3 cells showed a more pronounced tendency to form clusters when cultured on GelMA. As a reference line, SKOV3 retained a more elongated morphology compared to the HG-SOC cells, with this trait appearing more pronounced on the HAGel substrate.

3.6. Expression of Cell Receptors and Matrix-Remodeling Markers

The cell survival and growth in a 3D printed scaffold are also correlated to the proactive interactions between cell receptors and the hosting substrate. HA has been used as an active targeting agent for the selective recognition of OC cells by interacting with the surface protein cluster determinant 44 (receptor CD44). In this context, we evaluated the expression of CD44, along with other key receptors, such as the hyaluronan-mediated motility receptor (HMMR) and the intercellular adhesion molecule-1 (ICAM-1), in 2D culture as a reference for the 3D studies. CD44 is a principal hyaluronan receptor involved in cancer stemness and cell adhesion, whereas HMMR (also known as RHAMM) is involved in cytoskeletal remodeling and cell motility, and ICAM-1 is a key adhesion receptor mediating cell−cell and cell−matrix interactions, facilitating tumor cell adhesion, immune evasion, and metastatic dissemination.[49,50] qRT-PCR results showed that HMMR mRNA expression is comparable between the investigated cell lines; CD44 mRNA expression was higher in KURAMOCHI and SKOV3 cells, which displayed similar values. Conversely, ICAM1 mRNA was expressed at lower levels than the other receptors, with slightly higher expression levels in OVCAR3 cells (Figure 8a). Additionally, WB analysis confirmed the lower expression of CD44 proteins in OVCAR3 cells compared to KURAMOCHI and SKOV3 (Figure 8b).

Since HMMR expression was similar in all investigated HG-SOC lines while ICAM1 is expressed at lower levels in all cells, differences in CD44 expression could have relevance in viability achievements.

Considering that, in 3D bioprinted constructs, cellular responses could be influenced by the physicochemical and mechanical features of the supporting matrix, we analysed the expression of cell receptors and a set of cell adhesion- and matrix-remodeling markers with recognized relevance in HG-SOC progression (Figure 9 and Supporting Information). In detail, based on the preliminary 2D assessment of HA-related receptors, CD44 and ICAM1 were selected as the primary targets, as they provide direct insight into cell–matrix interactions. HMMR was not further investigated because its expression levels were comparable between the analyzed cell lines.

MMP-2 and MMP-14 were examined to assess the extent of matrix remodeling and the invasive potential driven by scaffold properties. OC progression relies heavily on the ability to degrade and remodel the ECM. We focused on MMP-2 and MMP-14 since they are critical drivers of this process, with their cooperative action being of particular importance.[51] MMP-14, a membrane-tethered protease, acts as an initiator, frequently located at the invasive fronts of tumor cells where it directly cleaves ECM components like collagen I and, crucially, activates the zymogen form of pro-MMP-2. This activation creates a powerful proteolytic cascade. The activated MMP-2 then efficiently degrades denatured collagens (gelatin) and key basement membrane components such as collagen IV, facilitating the breakdown of physical barriers to invasion. Beyond ECM degradation and cell invasion, the MMP-2/MMP-14 axis influences nearly every hallmark of OC, as cell adhesion molecules, angiogenesis and immune suppression. In parallel, E-cadherin was evaluated as an indicator of cell−cell adhesion and hallmark of the epithelial-to-mesenchymal transition (EMT), which may change as cells adapt to the 3D geometry. Together, these markers offer a representative snapshot of how

https://doi.org/10.1021/acsabm.6c00299
ACS Appl. Bio Mater. 2026, 9, 6370−6387

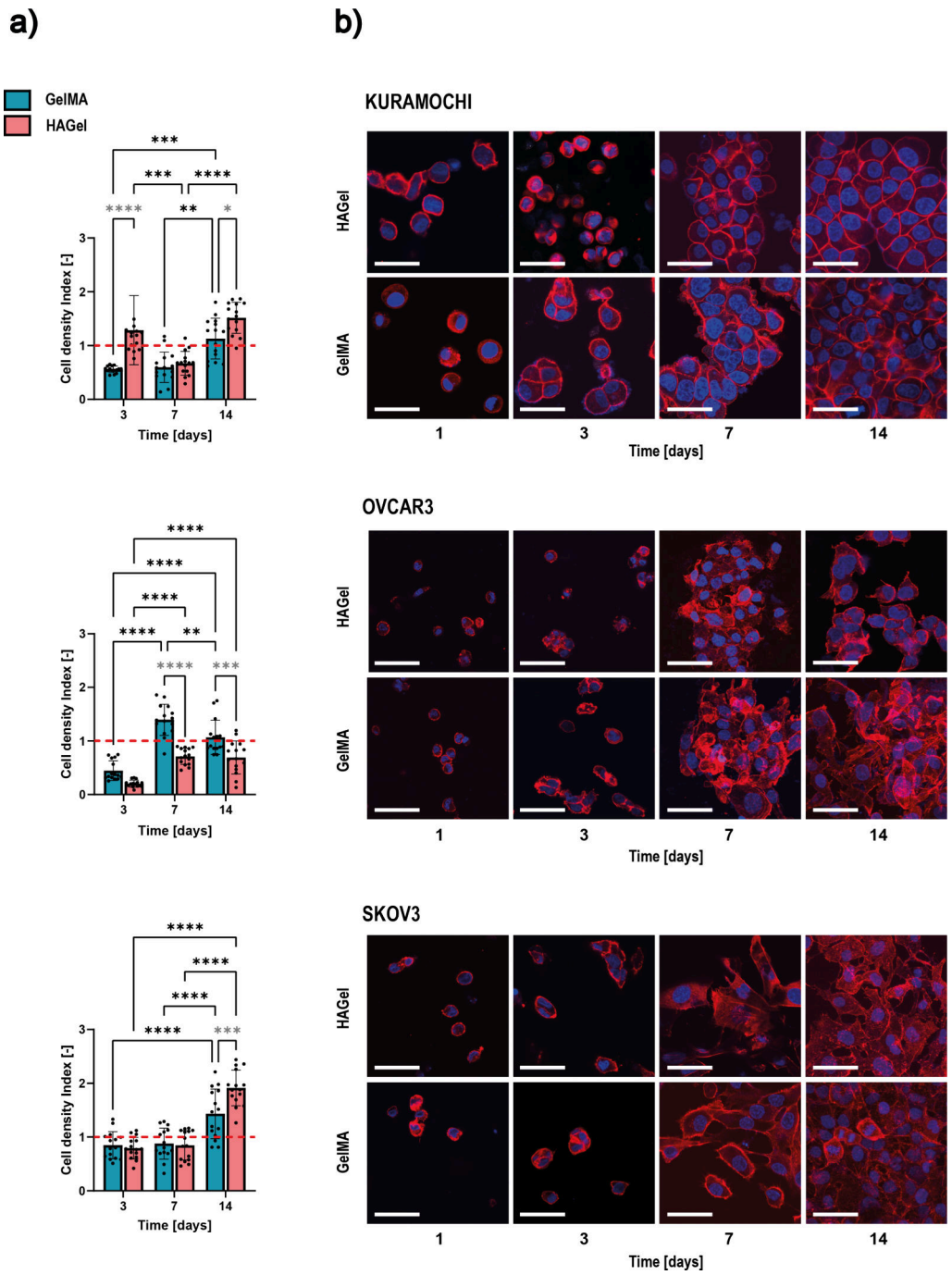

Figure 7. (a) Cell density over time. The red dotted line represents reference value after 1 day of culture. Statistical analysis was performed using two-way ANOVA. Significance at fixed time points is highlighted in gray, whereas significance between the two formulations is reported in black (significance levels are indicated as follows: $*p < 0.05$, $**p < 0.01$, $***p < 0.001$, $****p < 0.0001$). (b) Representative confocal images up to 14 days of culture of bioprinted constructs stained with phalloidin-TRITC (red, F-actin filaments) and Hoechst (blue, nuclei). Scale bar = 50 μm.

OVCAR3, KURAMOCHI, and SKOV3 cells sense and respond to printed substrates during early cultures.

Referring to Figure 9, KURAMOCHI showed a slight decrease in CD44 expression over time in the GelMA hydrogel, whereas its level remained stable in HAGel. In particular, at day 14, CD44 expression was significantly higher in the presence of HA ($p < 0.0001$). This behavior may reflect that the availability of HA within the matrix provides a physiological ligand able to sustain receptor engagement and avoid the downregulation. Interestingly, in HAGel, we observed a gradual increase in MMP-2 expression up to day 14 ($p < 0.0001$) higher than the corresponding counterpart in GelMA ($p < 0.05$), while MMP-14 remained essentially unchanged. This trend suggests an ECM-remodeling response consistent with HA-mediated signaling, in which cells modulate the interaction with the matrix and establish a favorable niche within the HAGel. In parallel, E-cadherin expression (Supporting Information Figure S5) exhibited a modest decrease from day 1 to day 14 in HAGel constructs, suggesting an active remodeling activity promoted by the HA-rich microenvironment.

https://doi.org/10.1021/acsabm.6c00299
ACS Appl. Bio Mater. 2026, 9, 6370−6387

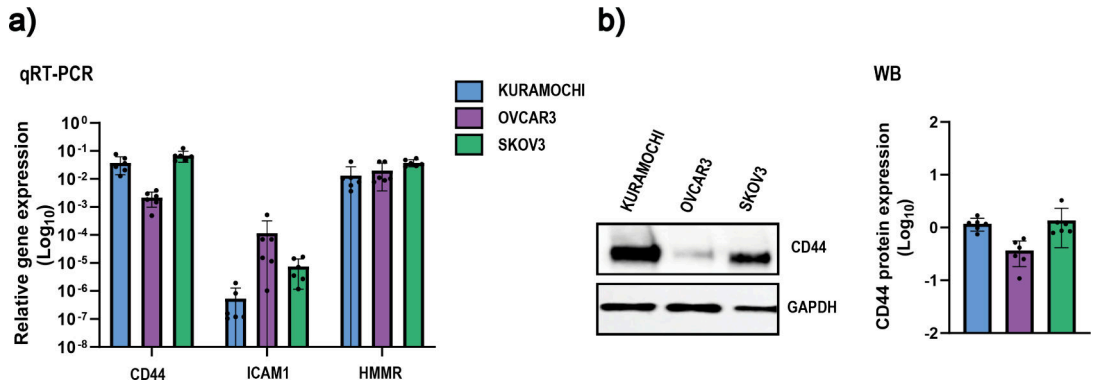

Figure 8. (a) qRT-PCR analysis of *CD44*, *ICAM1*, and *HMMR* mRNA expression in OC cell lines. Results are the mean ± SD of six independent experiments. (b) Representative WB analysis of CD44 expression in different OC cell lines. GAPDH was used as a loading control. Histograms, mean ± SD ($n = 6$).

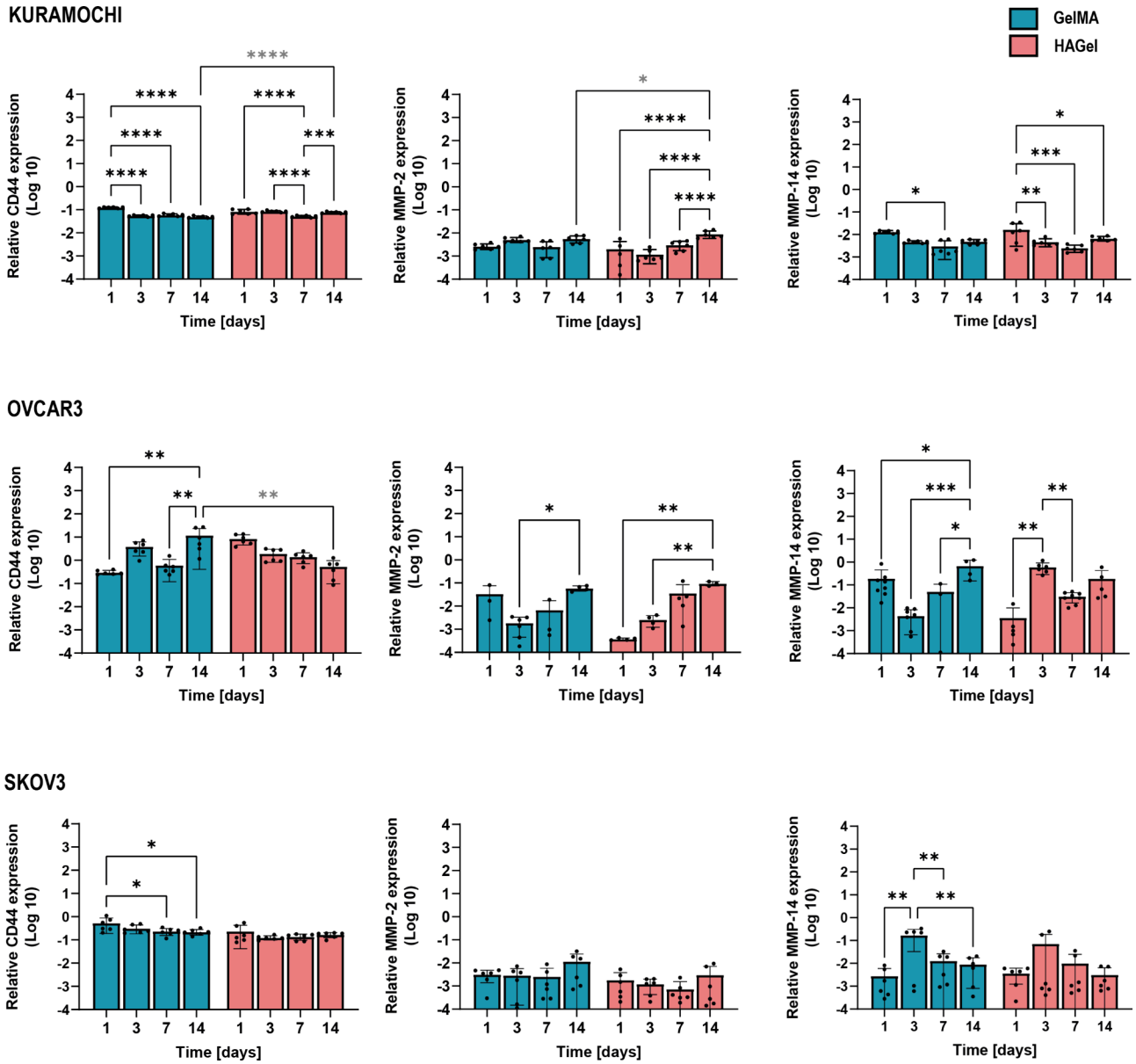

Figure 9. qRT-PCR analysis of CD44, MMP-2, and MMP-14 mRNA expression in investigated cell lines. Results are the mean ± SD of six independent experiments. Statistical analysis was performed via two-way ANOVA. Significance levels are indicated as follows: *$p < 0.05$, **$p < 0.01$, ***$p < 0.001$, ****$p < 0.0001$.

https://doi.org/10.1021/acsabm.6c00299
ACS Appl. Bio Mater. 2026, 9, 6370−6387

To further support these preliminary outcomes, we tested, as a representative scenario of a more complex in vitro tumoral microenvironment (TME), the 3D printing of a HAGel construct incorporating also human ovarian fibroblasts (HOFs) as discussed in Supporting Information Figure S6. In this context, epithelial markers typically show enhanced stabilization in the presence of fibroblasts, reflecting the contribution of stromal-derived factors in supporting epithelial cohesion within HA-rich matrices. Conversely, metalloproteinases often increase, as fibroblast-mediated paracrine pathways and ECM turnover synergize with tumor cells to promote a more dynamic remodeling activity. This highlighted the relevance of HAGel substrates for reproducing early stromal–tumor interactions.

For OVCAR3, an increase in CD44, MMP-2, and MMP-14 expression was observed from day 3 to day 14 in GelMA, while HAGel showed showed a slight decrease (although nonstatistically significant) in CD44 expression and a gradual increase in MMPs. As discussed in Section 3.5, the variability of data at day 1 could be ascribed to an impact of the extrusion-based printing process on cell response.

The upregulation of CD44 in GelMA might reflect an adaptive response to the 3D environment. GelMA provides a bioadhesive, collagen-I-rich matrix that structurally and biochemically mimics the native TME. In this context, increased CD44 expression likely enhances cellular anchorage and sensing through interactions with matrix components, independently of its canonical ligand HA. Concomitantly, a progressive downregulation of E-cadherin was detected from day 1 to day 14 (Figure S5). This loss of epithelial phenotype correlates with a gain invasive potential. This is further supported by the expression profile of MMPs. MMP-2 expression was significantly enhanced from day 3 onward, while the upregulation of MMP-14 was sustained through day 14. Because MMP-14 directly degrades ECM and activates pro-MMP-2, its sustained expression indicates a proteolytic phenotype supportive of cell invasion.

Overall, these observations suggest that OVCAR3 cells may adapt more favorably to a collagen-like environment such as GelMA than to an HA-rich matrix. In GelMA, OVCAR3 showed higher cell density and a molecular profile consistent with a more effective 3D adaptation.

While these results do not imply a universal preference, they highlight that matrix composition plays a role in shaping cell fitness and remodeling strategies in 3D and that GelMA constituted a more permissive substrate for OVCAR3 under the tested conditions.

As performed for the other HG-SOC cell line, we assessed a 3D printed construct incorporating layered OVCAR3 cells and HOFs to evaluate cell behavior in a more realistic TME-like scenario (Supporting Information). Our data provide evidence that HOFs act collaboratively with cancer cells to remodel the ECM. This stromal−epithelial cross talk was sufficient to maintain the upregulation of MMP-14, underscoring the role of the stromal compartment in sustaining the invasive capacity of cancer cells within this model.

Finally, for the reference cell line SKOV3, a slight decrease in CD44 expression was detected in GelMA ($p < 0.05$, day 1 vs day 14), while the level remained stable in HAGel. For MMPs, MMP-2 and MMP-14 showed a modest (nonsignificant) increase over time, whereas E-cadherin exhibited a comparable decreasing trend in both hydrogel formulations (Supporting Information). Despite the comparable expression trends, the higher cell density observed in HAGel suggests that SKOV3 may benefit from an HA-enriched microenvironment. This behavior is consistent with the intermediate grade and partial mesenchymal features of SKOV3, which make these cells less dependent on collagen-driven cues and more permissive toward HA-mediated matrix interactions.[52]

For all investigated cell lines, the expression of ICAM1 was lower (data not shown). Therefore, any speculation on the impact of ICAM1 on cell behavior or compartmentalization within the different 3D constructs would be limited and not particularly informative. Overall, the results for CD44 and the other markers suggest that, for HG-SOC cell lines, the presence of HA motifs in the matrix could improve the cell viability and growth for KURAMOCHI, while exerting a lower impact on OVCAR3 results. Indeed, in this case, the addition of HA did not provide an improvement in cell viability. For SKOV3, non-HG-SOC cells, the expression of key phenotypic markers showed minimal variation between HAGel and GelMA constructs. Nevertheless, the higher cell density observed in HAGel indicated a positive effect of HA on overall cell fitness and proliferation in this context.

These results highlighted that the formulation of hydrogels can influence adhesion, growth, and proliferation of HG-SOC cells within a 3D printed construct, particularly the presence of HA. Notably, HG-SOC cells are rarely used in 3D bioprinting studies, in contrast to other ovarian cancer cells, and our findings proved that by modifying the matrix composition, it is possible to provide a more suitable environment for specific cell lines of the HG-SOC, opening new possibilities for the 3D modeling.

4. CONCLUSIONS

In this work, we investigated the 3D bioprinting of HG-SOC cells and evaluated how HA, as a component of the bioink formulation, could affect the cell viability, proliferation, morphology, and marker expression over a 14 day culture period. Both GelMA, employed as a reference hydrogel formulation, and HAGel exhibited suitable rheological and mechanical properties for extrusion-based bioprinting, enabling reproducible fabrication of cell-laden constructs and supporting efficient cell encapsulation and growth. The optimization of the printing process allowed the identification of printing parameters for both bioinks, ensuring highly reproducible constructs. Water uptake and degradation analyses confirmed the structural stability of the printed hydrogels over time, with the incorporation of HA contributing to a mechanically reinforced network architecture, as reflected by increased stiffness and reduced deformability, also consistent with a more stable hydration profile and reduced degradation compared to GelMA.

On the other hand, considering the different expression of the specific cell receptors and markers involved in cell adhesion, motility, and proliferation, we can assess that a different HG-SOC cell response occurred in the presence of HA motifs in the 3D scaffold. In particular, KURAMOCHI cells exhibited higher viability and density in the presence of HAGel, consistent with a high expression of CD44 and the observed trends of E-cadherin and MMPs within the 3D construct. Conversely, OVCAR3 cells showed better results in the presence of gelatin only (i.e., GelMA scaffold). Although the differences in the expression of some of the investigated receptors were not extremely marked, the variations in cell growth suggested different substrate suitability.

Finally, SKOV3, used as OC reference cell line, exhibited improved viability in the presence of HA.

https://doi.org/10.1021/acsabm.6c00299
ACS Appl. Bio Mater. 2026, 9, 6370−6387

Overall, these findings could represent a guideline in the formulation of bioink and the fabrication of in vitro HG-SOC models, highlighting the importance of the rational choice of the starting polymers for the development of the 3D hydrogel scaffolds and paving the way for the design of advanced models of tumor microenvironment where the different types of cells can be hosted by the corresponding optimized cell niche.

■ ASSOCIATED CONTENT

Supporting Information

The Supporting Information is available free of charge at https://pubs.acs.org/doi/10.1021/acsabm.6c00299.

Representative scaffold images and ROI selection; ATR-FTIR spectra of GelMA and GMHA; ^{1}H NMR spectrum of GelMA and GMHA after UV irradiation; cell proliferative activity assays and related quantitative results; E-cadherin expression analysis; HG-SOC and HOF culture-layered bioprinting procedure, experimental details, and qRT-PCR analysis (DOCX)

Wettability of the GelMA-based scaffold (Video S1) (MP4)

Wettability of the HAGel scaffold (Video S2) (MP4)

■ AUTHOR INFORMATION

Corresponding Author

Emanuele Mauri − *Department of Chemistry, Materials, and Chemical Engineering "Giulio Natta", Politecnico di Milano, Piazza Leonardo da Vinci 32, Milan 20133, Italy;* orcid.org/0000-0002-6203-8405; Email: emanuele.mauri@polimi.it

Authors

Chiara Scrocciolani − *Department of Mechanical Engineering, Politecnico di Milano, Via La Masa 1, Milan 20156, Italy;* orcid.org/0009-0001-9022-6905

Leonardo Caserio − *Department of Chemistry, Materials, and Chemical Engineering "Giulio Natta", Politecnico di Milano, Piazza Leonardo da Vinci 32, Milan 20133, Italy;* orcid.org/0009-0004-7567-8358

Silvia Grillo − *National Research Council,Institute of Molecular Biology and Pathology, Via degli Apuli 4, Rome 00185, Italy*

Flavia Ottavi − *National Research Council,Institute of Molecular Biology and Pathology, Via degli Apuli 4, Rome 00185, Italy*

Ilenia Masi − *National Research Council,Institute of Molecular Biology and Pathology, Via degli Apuli 4, Rome 00185, Italy;* orcid.org/0000-0001-8927-1998

Emanuela Jacchetti − *Department of Chemistry, Materials, and Chemical Engineering "Giulio Natta", Politecnico di Milano, Piazza Leonardo da Vinci 32, Milan 20133, Italy*

Francesco Briatico Vangosa − *Department of Chemistry, Materials, and Chemical Engineering "Giulio Natta", Politecnico di Milano, Piazza Leonardo da Vinci 32, Milan 20133, Italy;* orcid.org/0000-0002-7088-1064

Manuela Teresa Raimondi − *Department of Chemistry, Materials, and Chemical Engineering "Giulio Natta", Politecnico di Milano, Piazza Leonardo da Vinci 32, Milan 20133, Italy*

Bianca Maria Colosimo − *Department of Mechanical Engineering, Politecnico di Milano, Via La Masa 1, Milan 20156, Italy*

Laura Rosanò − *National Research Council,Institute of Molecular Biology and Pathology, Via degli Apuli 4, Rome 00185, Italy;* orcid.org/0000-0002-9962-6411

Davide Moscatelli − *Department of Chemistry, Materials, and Chemical Engineering "Giulio Natta", Politecnico di Milano, Piazza Leonardo da Vinci 32, Milan 20133, Italy;* orcid.org/0000-0003-2759-9781

Complete contact information is available at: https://pubs.acs.org/doi/10.1021/acsabm.6c00299

Author Contributions

†C.S. and L.C. contributed equally to this work.

Notes

The authors declare no competing financial interest.

■ ACKNOWLEDGMENTS

E.M. and L.R. are supported by PRIN 2022 PNRR-European Union–Next Generation EU, Mission 4, Component 1, project number P2022Z7TEC. M.T.R. is supported by the European Research Council (call ERC-AdG-2021, project BEACONSANDEGG, G.A. 101053122). L.R. is supported by Banca D'Italia, Contributo Liberale 2024. I.M. is a recipient of a fellowship from the Italian Foundation for Cancer Research. The authors gratefully acknowledge Carl ZEISS S.p.A. for providing access to the confocal imaging system (ZEISS Axio Observer 7 with Line Rescan NL5+ Confocal NL) used for the acquisition of Figure S1c (Supporting Information). We thank Dr. Riccardo Tognato for their technical support and assistance during image acquisition.

■ SYMBOLS

DoF_{GelMA}	degree of functionalization GelMA
DoF_{HAGel}	degree of functionalization HAGel
T_{gGelMA}	gelation temperature GelMA
T_{gHAGel}	gelation temperature HAGel
T_g	sol−gel transition temperature
G'	storage modulus
G''	loss modulus
ω	angular frequency
$\dot{\gamma}$	shear rate
τ_y	yield stress
τ_f	flow point
$\lvert\eta^*\rvert$	complex viscosity
w_{wet}	wet weight
w_{dry}	dry weight

■ REFERENCES

(1) Bray, F.; Laversanne, M.; Sung, H.; Ferlay, J.; Siegel, R. L.; Soerjomataram, I.; Jemal, A. Global Cancer Statistics 2022: GLOBOCAN Estimates of Incidence and Mortality Worldwide for 36 Cancers in 185 Countries. *CA Cancer J. Clin.* **2024**, *74* (3), 229–263.

(2) Poornima, K.; Francis, A. P.; Hoda, M.; Eladl, M. A.; Subramanian, S.; Veeraraghavan, V. P.; El-Sherbiny, M.; Asseri, S. M.; Hussamuldin, A. B. A.; Surapaneni, K. M.; Mony, U.; Rajagopalan, R. Implications of Three-Dimensional Cell Culture in Cancer Therapeutic Research. *Front. Oncol.* **2022**, *12*, No. 891673.

(3) Ma, Y.; Xue, F.; Pei, Z.; Zhao, Y. Constructing a Co-Culture Model of Cancer-Associated Fibroblasts and Ovarian Cancer Organoids and Studying Mechanisms of Drug Resistance. *Exp. Cell Res.* **2025**, *450* (2), No. 114656.

https://doi.org/10.1021/acsabm.6c00299
ACS Appl. Bio Mater. 2026, 9, 6370−6387

(4) Paradiso, F.; Lenna, S.; Gazze, S. A.; Parra, J. G.; Murphy, K.; Margarit, L.; Gonzalez, D.; Francis, L.; Taraballi, F. Mechanomimetic 3D Scaffolds as a Humanized In Vitro Model for Ovarian Cancer. *Cells* **2022**, *11* (5), No. 824.
(5) Wu, T.; Gao, Y. Y.; Su, J.; Tang, X. N.; Chen, Q.; Ma, L. W.; Zhang, J. J.; Wu, J. M.; Wang, S. X. Three-Dimensional Bioprinting of Artificial Ovaries by an Extrusion-Based Method Using Gelatin-Methacryloyl Bioink. *Climacteric* **2022**, *25* (2), 170–178.
(6) Shin, S.; Ikram, M.; Subhan, F.; Kang, H. Y.; Lim, Y.; Lee, R.; Jin, S.; Jeong, Y. H.; Kwak, J. Y.; Na, Y. J.; Yoon, S. Alginate-Marine Collagen-Agarose Composite Hydrogels as Matrices for Biomimetic 3D Cell Spheroid Formation. *RSC Adv.* **2016**, *6* (52), 46952–46965.
(7) Zhou, N.; Ma, X.; Hu, W.; Ren, P.; Zhao, Y.; Zhang, T. Effect of RGD Content in Poly(Ethylene Glycol)-Crosslinked Poly(Methyl Vinyl Ether-Alt-Maleic Acid) Hydrogels on the Expansion of Ovarian Cancer Stem-like Cells. *Mater. Sci. Eng. C* **2021**, *118*, No. 111477.
(8) Zhou, N.; Ma, X.; Bernaerts, K. V.; Ren, P.; Hu, W.; Zhang, T. Expansion of Ovarian Cancer Stem-like Cells in Poly(Ethylene Glycol)-Cross-Linked Poly(Methyl Vinyl Ether- A Lt-Maleic Acid) and Alginate Double-Network Hydrogels. *ACS Biomater. Sci. Eng.* **2020**, *6* (6), 3310–3326.
(9) Woo, M. M. M.; Salamanca, C. M.; Minor, A.; Auersperg, N. An Improved Assay to Quantitate the Invasiveness of Cells in Modified Boyden Chambers. *In Vitro Cell. Dev. Biol. Anim.* **2007**, *43* (1), 7–9.
(10) Sodek, K. L.; Brown, T. J.; Ringuette, M. J. Collagen I but Not Matrigel Matrices Provide an MMP-Dependent Barrier to Ovarian Cancer Cell Penetration. *BMC Cancer* **2008**, *8* (1), No. 223.
(11) Evans, C. L.; Abu-Yousif, A. O.; Park, Y. J.; Klein, O. J.; Celli, J. P.; Rizvi, I.; Zheng, X.; Hasan, T. Killing Hypoxic Cell Populations in a 3D Tumor Model with EtNBS-PDT. *PLoS One* **2011**, *6* (8), No. e23434.
(12) Liu, M.; Zhang, X.; Long, C.; Xu, H.; Cheng, X.; Chang, J.; Zhang, C.; Zhang, C.; Wang, X. Collagen-Based Three-Dimensional Culture Microenvironment Promotes Epithelial to Mesenchymal Transition and Drug Resistance of Human Ovarian Cancer in vitro. *RSC Adv.* **2018**, *8* (16), 8910–8919.
(13) Tan, B.; Gan, S.; Wang, X.; Liu, W.; Li, X. Applications of 3D Bioprinting in Tissue Engineering: Advantages, Deficiencies, Improvements, and Future Perspectives. *J. Mater. Chem. B* **2021**, *9* (27), 5385–5413.
(14) Kang, Y.; Datta, P.; Shanmughapriya, S.; Ozbolat, I. T. 3D Bioprinting of Tumor Models for Cancer Research. *ACS Appl. Bio Mater.* American Chemical Society **2020**, *3* (9), 5552–5573.
(15) Datta, P.; Dey, M.; Ataie, Z.; Unutmaz, D.; Ozbolat, I. T. 3D Bioprinting for Reconstituting the Cancer Microenvironment. *NPJ Precis. Oncol.* **2020**, *4*, No. 18.
(16) Xu, F.; Celli, J.; Rizvi, I.; Moon, S.; Hasan, T.; Demirci, U. A Three-Dimensional in Vitro Ovarian Cancer Coculture Model Using a High-Throughput Cell Patterning Platform. *Biotechnol. J.* **2011**, *6* (2), 204–212.
(17) Baka, Z.; Godier, C.; Lamy, L.; Mallick, A.; Gribova, V.; Figarol, A.; Bezdetnaya, L.; Chateau, A.; Magne, Z.; Stiefel, M.; Louaguef, D.; Lavalle, P.; Gaffet, E.; Joubert, O.; Alem, H. A Coculture Based, 3D Bioprinted Ovarian Tumor Model Combining Cancer Cells and Cancer Associated Fibroblasts. *Macromol. Biosci.* **2023**, *23* (3), No. 2200434.
(18) Cao, H.; Duan, L.; Zhang, Y.; Cao, J.; Zhang, K. Current Hydrogel Advances in Physicochemical and Biological Response-Driven Biomedical Application Diversity. *Signal Transduction Targeted Ther.* **2021**, *6* (1), No. 426.
(19) Elango, J.; Zamora-Ledezma, C. Rheological, Structural, and Biological Trade-Offs in Bioink Design for 3D Bioprinting. *Gels* **2025**, *11* (8), No. 659.
(20) Chai, C.; Liang, L.; Mikkelsen, N. S.; Wang, W.; Zhao, W.; Sun, C.; Bak, R. O.; Li, H.; Lin, L.; Wang, F.; Luo, Y. Single-Cell Transcriptome Analysis of Epithelial, Immune, and Stromal Signatures and Interactions in Human Ovarian Cancer. *Commun. Biol.* **2024**, *7* (1), No. 131.
(21) Cho, A.; Howell, V. M.; Colvin, E. K. The Extracellular Matrix in Epithelial Ovarian Cancer - A Piece of a Puzzle. *Front. Oncol.* **2015**, *5* (245), No. 245.
(22) Pape, J.; Cheema, U.; Tocci, P.; Sestito, R.; Masi, I.; Loizidou, M.; Bagnato, A.; Rosanò, L. Endothelin-1 Receptor Blockade Impairs Invasion Patterns in Engineered 3D High-Grade Serous Ovarian Cancer Tumouroids. *Clin. Sci.* **2024**, *138* (22), 1441–1450.
(23) Kramer, M.; Criswell, A.; Marzette, K.; Cutcliffe, E.; Sewell-Loftin, M. K. Strain and Hyaluronic Acid Interact to Regulate Ovarian Cancer Cell Proliferation, Migration, and Drug Resistance. *Mechanobiol. Med.* **2024**, *2* (4), No. 100094.
(24) Liu, Z.; Hou, P.; Fang, J.; Shao, C.; Shi, Y.; Melino, G.; Peschiaroli, A. Hyaluronic Acid Metabolism and Chemotherapy Resistance: Recent Advances and Therapeutic Potential. *Mol. Oncol.* **2024**, *18*, 2087−2106.
(25) Torre, M.; Giannitelli, S. M.; Mauri, E.; Gori, M.; Bucciarelli, A.; Mozetic, P.; Gigli, G.; Trombetta, M.; Rainer, A. Printability Assessment Workflow of a Thermosensitive Photocurable Biomaterial Ink for Microextrusion Bioprinting. *Bioprinting* **2023**, *30*, No. e00262.
(26) Sigen, A.; Xu, Q.; McMichael, P.; Gao, Y.; Li, X.; Wang, X.; Greiser, U.; Zhou, D.; Wang, W. A Facile One-Pot Synthesis of Acrylated Hyaluronic Acid. *Chem. Commun.* **2018**, *54* (9), 1081–1084.
(27) Lai, T. C.; Yu, J.; Tsai, W. B. Gelatin Methacrylate/Carboxybetaine Methacrylate Hydrogels with Tunable Crosslinking for Controlled Drug Release. *J. Mater. Chem. B* **2016**, *4* (13), 2304–2313.
(28) Zanderigo, G.; Bracco, F.; Semeraro, Q.; Colosimo, B. M. In-Situ Printability Maps (IPM): A New Approach for in-Situ Printability Assessment with Application to Extrusion-Based Bioprinting. *Bioprinting* **2023**, *36*, No. e00320.
(29) Rastin, H.; Ormsby, R. T.; Atkins, G. J.; Losic, D. 3D Bioprinting of Methylcellulose/Gelatin-Methacryloyl (MC/GelMA) Bioink with High Shape Integrity. *ACS Appl. Bio Mater.* **2020**, *3* (3), 1815–1826.
(30) Choi, J. B.; Kim, Y. K.; Byeon, S. M.; Park, J. E.; Bae, T. S.; Jang, Y. S.; Lee, M. H. Characteristics of Biodegradable Gelatin Methacrylate Hydrogel Designed to Improve Osteoinduction and Effect of Additional Binding of Tannic Acid on Hydrogel. *Polymers* **2021**, *13* (15), No. 2535.
(31) Kilic Bektas, C.; Hasirci, V. Cell Loaded GelMA:HEMA IPN Hydrogels for Corneal Stroma Engineering. *J. Mater. Sci.:Mater. Med.* **2020**, *31* (1), No. 2.
(32) Sochilina, A. V.; Savelyev, A. G.; Akasov, R. A.; Zubov, V. P.; Khaydukov, E. V.; Generalova, A. N. Preparing Modified Hyaluronic Acid with Tunable Content of Vinyl Groups for Use in Fabrication of Scaffolds by Photoinduced Crosslinking. *Russ. J. Bioorg. Chem.* **2021**, *47* (4), 828–836.
(33) Bencherif, S. A.; Srinivasan, A.; Horkay, F.; Hollinger, J. O.; Matyjaszewski, K.; Washburn, N. R. Influence of the Degree of Methacrylation on Hyaluronic Acid Hydrogels Properties. *Biomaterials* **2008**, *29* (12), 1739–1749.
(34) Liu, W.; Heinrich, M. A.; Zhou, Y.; Akpek, A.; Hu, N.; Liu, X.; Guan, X.; Zhong, Z.; Jin, X.; Khademhosseini, A.; Zhang, Y. S. Extrusion Bioprinting of Shear-Thinning Gelatin Methacryloyl Bioinks. *Adv. Healthcare Mater.* **2017**, *6* (12), No. 1601451.
(35) Kaemmerer, E.; Melchels, F. P. W.; Holzapfel, B. M.; Meckel, T.; Hutmacher, D. W.; Loessner, D. Gelatine Methacrylamide-Based Hydrogels: An Alternative Three-Dimensional Cancer Cell Culture System. *Acta Biomater.* **2014**, *10* (6), 2551–2562.
(36) Fu, Z.; Hai, N.; Zhong, Y.; Sun, W. Printing GelMA Bioinks: A Strategy for Building in Vitro Model to Study Nanoparticle-Based Minocycline Release and Cellular Protection under Oxidative Stress. *Biofabrication* **2024**, *16* (2), No. 025040.
(37) Ermis, M.; Falcone, N.; Roberto de Barros, N.; Mecwan, M.; Haghniaz, R.; Choroomi, A.; Monirizad, M.; Lee, Y.; Song, J.; Cho, H. J.; Zhu, Y.; Kang, H.; Dokmeci, M. R.; Khademhosseini, A.; Lee, J.; Kim, H. J. Tunable Hybrid Hydrogels with Multicellular Spheroids for Modeling Desmoplastic Pancreatic Cancer. *Bioact. Mater.* **2023**, *25*, 360–373.
(38) Camci-Unal, G.; Cuttica, D.; Annabi, N.; Demarchi, D.; Khademhosseini, A. Synthesis and Characterization of Hybrid Hyaluronic Acid-Gelatin Hydrogels. *Biomacromolecules* **2013**, *14* (4), 1085–1092.
(39) Shi, J.; Xing, M. M. Q.; Zhong, W. Development of Hydrogels and Biomimetic Regulators as Tissue Engineering Scaffolds. *Membranes* **2012**, *2* (1), 70−90.

https://doi.org/10.1021/acsabm.6c00299
ACS Appl. Bio Mater. 2026, 9, 6370−6387

(40) Alizadeh, M.; Abbasi, F.; Khoshfetrat, A. B.; Ghaleh, H. Microstructure and Characteristic Properties of Gelatin/Chitosan Scaffold Prepared by a Combined Freeze-Drying/Leaching Method. *Mater. Sci. Eng. C* **2013**, *33* (7), 3958–3967.
(41) Yue, K.; Trujillo-de Santiago, G.; Alvarez, M. M.; Tamayol, A.; Annabi, N.; Khademhosseini, A. Synthesis, Properties, and Biomedical Applications of Gelatin Methacryloyl (GelMA) Hydrogels. *Biomaterials* **2015**, *73*, 254−271.
(42) Velasco- Rodriguez, B.; Diaz-vidal, T.; Rosales-rivera, L. C.; García-gonzález, C. A.; Alvarez-lorenzo, C.; Al-modlej, A.; Domínguez-arca, V.; Prieto, G.; Barbosa, S.; Soltero Martínez, J. F. A.; Taboada, P. Hybrid Methacrylated Gelatin and Hyaluronic Acid Hydrogel Scaffolds. Preparation and Systematic Characterization for Prospective Tissue Engineering Applications. *Int. J. Mol. Sci.* **2021**, *22* (13), No. 6758.
(43) Wu, Y.; Zhao, S.; Wang, J.; Chen, Y.; Li, H.; Li, J.-P.; Kan, Y.; Zhang, T. Methods for Determining the Structure and Physicochemical Properties of Hyaluronic Acid and Its Derivatives: A Review. *Int. J. Biol. Macromol.* **2024**, *282* (Pt 6), 137603−137603.
(44) Yang, J.; Rong, Y.; Chen, X.; He, C. Hydrogel Scaffolds with Controlled Postgelation Modulation of Structures for 3D Cell Culture and Tissue Engineering. *Macromol. Chem. Phys.* **2024**, *225* (5), No. 2300365.
(45) Graham, O.; Rodriguez, J.; van Biljon, L.; Fashemi, B.; Graham, E.; Fuh, K.; Khabele, D.; Mullen, M. Generation and Culturing of High-Grade Serous Ovarian Cancer Patient-Derived Organoids. *J. Visualized Exp.* **2023**, (191), No. e64878.
(46) Hallas-Potts, A.; Dawson, J. C.; Herrington, C. S. Ovarian Cancer Cell Lines Derived from Non-Serous Carcinomas Migrate and Invade More Aggressively than Those Derived from High-Grade Serous Carcinomas. *Sci. Rep.* **2019**, *9* (1), No. 5515.
(47) Elias, K. M.; Emori, M. M.; Papp, E.; Macduffie, E.; Konecny, G. E.; Velculescu, V. E.; Drapkin, R. Beyond Genomics: Critical Evaluation of Cell Line Utility for Ovarian Cancer Research. *Gynecol. Oncol.* **2015**, *139* (1), 97–103.
(48) Heredia-Soto, V.; Redondo, A.; Berjón, A.; Miguel-Martín, M.; Díaz, E.; Crespo, R.; Hernández, A.; Yébenes, L.; Gallego, A.; Feliu, J.; Hardisson, D.; Mendiola, M. High-Throughput 3-Dimensional Culture of Epithelial Ovarian Cancer Cells as Preclinical Model of Disease *Oncotarget* **2018**, *9* (31), 21893–21903.
(49) Qiu, Z.; Wang, Y.; Zhang, Z.; Qin, R.; Peng, Y.; Tang, W.; Xi, Y.; Tian, G.; Zhang, Y. Roles of Intercellular Cell Adhesion Molecule-1 (ICAM-1) in Colorectal Cancer: Expression, Functions, Prognosis, Tumorigenesis, Polymorphisms and Therapeutic Implications. *Front. Oncol.* **2022**, *12*, No. 1052672.
(50) Misra, S.; Hascall, V. C.; Markwald, R. R.; Ghatak, S. Interactions between Hyaluronan and Its Receptors (CD44, RHAMM) Regulate the Activities of Inflammation and Cancer. *Front. Immunol.* **2015**, *6* (201), No. 31.
(51) Carey, P.; Low, E.; Harper, E.; Stack, M. S. Metalloproteinases in Ovarian Cancer. *Int. J. Mol. Sci.* **2021**, *22* (7), No. 3403.
(52) Strauss, R.; Li, Z. Y.; Liu, Y.; Beyer, I.; Persson, J.; Sova, P.; Möller, T.; Pesonen, S.; Hemminki, A.; Hamerlik, P.; Drescher, C.; Urban, N.; Bartek, J.; Lieber, A. Analysis of Epithelial and Mesenchymal Markers in Ovarian Cancer Reveals Phenotypic Heterogeneity and Plasticity. *PLoS One* **2011**, *6* (1), No. e16186.

https://doi.org/10.1021/acsabm.6c00299
ACS Appl. Bio Mater. 2026, 9, 6370−6387